Finescale Orographic Precipitation Variability and Gap-Filling Radar Potential in Little Cottonwood Canyon, Utah

LEAH S. CAMPBELL AND W. JAMES STEENBURGH

Department of Atmospheric Sciences, University of Utah, Salt Lake City, Utah

ABSTRACT

Finescale variations in orographic precipitation pose a major challenge for weather prediction, winter road maintenance, and avalanche forecasting and mitigation in mountainous regions. In this investigation, ground-based X-band radar observations collected during intensive observing period 6 (IOP6) of the Storm Chasing Utah Style Study (SCHUSS) are used to provide an example of these variations during a winter storm in the Wasatch Mountains of northern Utah. Emphasis is placed on precipitation features in and around Little Cottonwood Canyon (LCC), which cuts orthogonally eastward into the central Wasatch Mountains. Precipitation during the weakly stratified prefrontal storm stage featured a wavelike barrier-scale reflectivity maximum over the Wasatch Crest and upper LCC that extended weakly westward along the transverse ridges flanking LCC. This precipitation pattern appeared to reflect a veering wind profile, with southwesterly flow over the transverse ridges but cross-barrier westerly flow farther aloft. Sublimation within dry subcloud air further diminished low-level radar reflectivities over lower LCC. In contrast, the cold-frontal stage was associated with stronger reflectivities over lower LCC and the adjoining north- to northwest-facing canyon wall, consistent with shallow, northwesterly upslope flow. These results highlight the finescale precipitation variations that can occur during winter storms in complex terrain and demonstrate the potential for improved analysis and forecasting of precipitation in LCC using a gap-filling radar.

1. Introduction

Finescale (1–10 km) variations in precipitation over areas of highly variable three-dimensional topography pose a significant challenge for weather and climate prediction, hydrologic forecasting, avalanche mitigation, and winter road maintenance in mountainous regions (e.g., Meyers and Steenburgh 2013; Moreno et al. 2013). Interactions between the large-scale flow, regional topography, and local terrain features can create dramatic variations in precipitation rate and structure over small spatial scales during individual storms (Sinclair et al. 1997; Steenburgh 2003; Smith et al. 2003; Minder et al. 2008; Molinié et al. 2012; Moreno et al. 2013), as well as over climatological time periods (e.g., Frei and Schär 1998; Anders et al. 2007). Although much of the research examining orographic precipitation has concentrated on barrier-scale effects, especially windward

enhancement processes, the influence of smaller-scale topographic features (e.g., ridge–valley corrugations) and more complex terrain geometries has received less attention (Minder et al. 2008).

The dynamical and microphysical processes that affect the distribution and intensity of orographic precipitation vary with the dynamics and thermodynamics of the incipient airflow, the size and shape of the terrain, and the time scales controlling the growth and fallout of precipitation particles [see Roe (2005), Smith (2006), Houze (2012), Colle et al. (2013), and Stoelinga et al. (2013) for recent reviews]. Over the western United States, many orographic storms evolve through stable, transitional (frequently with frontal characteristics), and unstable stages (e.g., Hobbs 1975; Marwitz 1980; Cooper and Saunders 1980; Long et al. 1990; Sassen et al. 1990; Medina et al. 2007). The stable and unstable stages are roughly analogous to the "flow around" and "flow over" regimes emphasized by Rotunno and Houze (2007).

During the stable stage, the low-level flow is often blocked, resulting in an upstream pool of stagnant air or a barrier jet. Increased low-level stability due to sublimational or evaporative cooling can also contribute to flow

Corresponding author address: Leah S. Campbell, Dept. of Atmospheric Sciences, University of Utah, 135 South 1460 East, Rm. 819, Salt Lake City, UT 84112.
E-mail: leah.campbell@utah.edu

blocking, as has been observed upstream of the Wasatch Mountains of northern Utah (Colle et al. 2005; Cox et al. 2005), and create downslope or down-valley flow within canyons and valleys (Hill 1978; Bousquet and Smull 2003; Steiner et al. 2003). The ascent of incident air over the blocked flow can enhance precipitation as much as 100–150 km upstream of the initial mountain slope (Peterson et al. 1991; Houze et al. 2001). In some cases, strong vertical wind shear and turbulence near the top of the blocked air mass may contribute to precipitation generation (Medina et al. 2005; Houze and Medina 2005).

Precipitation processes during the stable stage can also be influenced by barrier- and subbarrier-scale mountain waves, the latter produced by ridge–valley corrugations in the topography. Klimowski et al. (1998), Bruintjes et al. (1994), and Reinking et al. (2000) found that small-scale ridges along Arizona's Mogollon Rim generate gravity waves that modulate the distribution of cloud liquid water and precipitation during winter storms. Colle (2004) showed that the reduced upstream tilt of gravity waves over narrow barriers (~25 km half-width) results in precipitation fallout over the crest and spill-over to the lee. Colle (2008) used two-dimensional simulations to show that a series of windward ridges can enhance precipitation over each ridge crest by a factor of 2–3 when the ridge spacing is relatively small (~20 km) and there is strong cross-barrier flow. Over the Cascade Mountains during the second Improvement of Microphysical Parameterization through Observational Verification Experiment (IMPROVE-2), a synergistic effect was found between barrier-scale mountain waves produced by midlevel cross-barrier flow and small-scale mountain waves formed by along-barrier flow over ridge–valley corrugations. This led to greater cloud liquid water production, hydrometeor mixing ratios, and precipitation rates over the subbarrier-scale windward ridges (Garvert et al. 2005, 2007).

The transitional stage can feature a sharp cold-frontal passage (Long et al. 1990; Sassen et al. 1990), a gradual transition in storm structure (Marwitz 1980), or a surge of low equivalent potential temperature θ_e air aloft that destabilizes the prefrontal environment, leading to convection (Reynolds and Kuciauskas 1988; Steenburgh 2003). The release of potential instability generated by surges of low-θ_e air aloft or differential θ_e advection ahead of a surface cold front frequently contributes to orographic precipitation enhancement, especially when coupled with the seeder–feeder process (Browning et al. 1974). Enhanced water vapor fluxes accompanying the prefrontal low-level jet can also contribute to strong orographic precipitation enhancement (Lin et al. 2001; Neiman et al. 2002; White et al. 2003; Neiman et al. 2008). Narrow cold-frontal precipitation bands can

exhibit changes in intensity, shape, and orientation as they interact with topographic obstacles (Braun et al. 1997; Colle et al. 1999; Yu and Smull 2000; Colle et al. 2002; Neiman et al. 2004; Bond et al. 2005; Viale et al. 2013).

The unstable storm stage is frequently characterized by orographically initiated or enhanced convection (e.g., Hobbs 1975). Reynolds and Kuciauskas (1988) and Peterson et al. (1991) found that, following cold-frontal passage in the Sierra Nevada, dry air tends to move in aloft with the resulting potential instability released as shallow convection when the flow surmounts the mountain barrier. Over the Oregon Cascades, Medina et al. (2007) showed that the "late sector" of extratropical cyclones generally consists of shallow convective echoes, which broaden as they move over the mountain barrier. This was also observed during IMPROVE-2 when post-frontal convective cells strengthened and upstream precipitation became more persistent during flow over the Cascade Mountains (Woods et al. 2005). Although not occurring exclusively in postfrontal or cold-sector environments, a variety of banded, cellular, and mesoscale precipitation features are generated or modified during unstable or potentially unstable flow interaction with complex terrain (e.g., Maddox et al. 1978; Caraceña et al. 1979; Parsons and Hobbs 1983; Sénési et al. 1996; Kirshbaum and Durran 2005; Kirshbaum et al. 2007; Godart et al. 2011).

The rich spectrum of storm environments, incident flow characteristics, topographic shapes and geometries, and dynamical and microphysical processes described above complicates precipitation forecasting and frequently leads to large intra- and interstorm variations in precipitation intensity and distribution (e.g., Steenburgh 2003). Often these variations occur at meso-γ (2–20 km) or even micro-α (200 m–2 km) scales (e.g., Rangno 1986; Neiman et al. 2002; Minder et al. 2008; Reuder et al. 2007) and are inadequately observed by operational radars or precipitation-gauge networks (e.g., Westrick et al. 1999; Wood et al. 2003; Beck and Bousquet 2013). Although high-resolution modeling systems are increasingly able to capture climatological precipitation gradients in mountainous regions (e.g., Ikeda et al. 2010), they frequently produce large errors during individual storms (e.g., Minder et al. 2008).

In this paper, we use observations collected by a mobile X-band radar to illustrate the finescale nature of precipitation features produced during a winter storm in an area of highly variable three-dimensional topography: the central Wasatch Mountains of northern Utah (Fig. 1a). The central Wasatch Mountains contain a system of ridges (Alpine, Cottonwood, and Wildcat) and canyons [Little Cottonwood (LCC), Big Cottonwood, and Mill Creek] that are oriented from west to east,
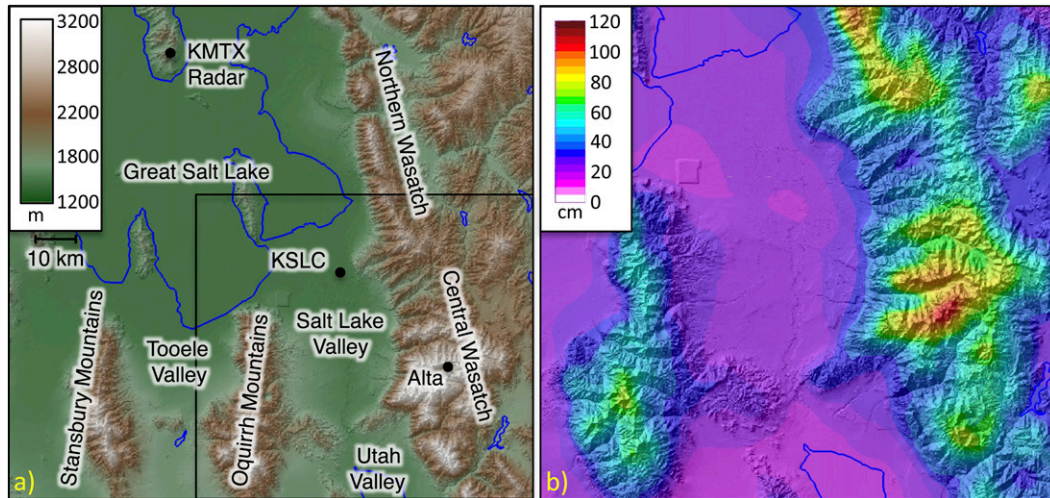
FIG. 1. (a) Topography and landmarks of the study region. (b) Mean cool-season (November–April) liquid equivalent precipitation (cm; following scale at left) within the inset box in the bottom right-hand corner of (a). [Data source is PRISM Climate Group, Oregon State University (http://prism.oregonstate.edu), created 18 Jun 2013.]

orthogonal to the predominantly north–south-oriented Wasatch Crest (Fig. 2a). Although the Wasatch Crest forms a hydrologic divide near the eastern termini of these canyons, the highest terrain is found along the Alpine and Cottonwood Ridges, which flank the deep, glacially carved LCC. Lone Peak (3430 m MSL; all subsequent elevations are MSL unless otherwise specified) and Twin Peaks (3453 m) create the westernmost abutments of the Alpine and Cottonwood Ridges, respectively, and dominate the Salt Lake Valley (SLV) skyline (Fig. 2b).

Dramatic climatological gradients in precipitation are found over the central Wasatch Mountains (Fig. 1b; Dunn 1983). A National Weather Service Cooperative Observer Program (COOP) observing site at Alta (2661 m) in upper LCC averages ~96 cm of liquid equivalent precipitation during the cool season (November–April), whereas Salt Lake City International Airport (KSLC, 1286 m; see Fig. 1a for location) in the northern SLV averages only ~23 cm (Western Regional Climate Center 2013). Estimates produced by the Parameter-Elevation Regression on Independent Slopes Model (PRISM) Climate Group at Oregon State University (Daly et al. 1994) suggest an increase in cool-season liquid equivalent precipitation from ~36 cm at the base of LCC to ~105 cm along the Alpine Ridge (Fig. 1b).

The winter storm examined in this paper was sampled during intensive observing period 6 (IOP6; from 0900 UTC 12 November to 0400 UTC 13 November 2011) of the Storm Chasing Utah Style Study (SCHUSS), a radar education and outreach field campaign involving the University of Utah and the Center for Severe Weather Research (CSWR). During IOP6, University of Utah students operated the CSWR Doppler on Wheels 6 (DOW6)

in the southwest corner of the SLV (see Fig. 2a for location) where a mostly unobstructed view of LCC and the western face of the central Wasatch Mountains allowed for detailed observation of precipitation features shaped by multiscale mountain waves and front–mountain interactions. State Route 210 (SR-210), which runs the length of LCC, services two of Utah's most popular ski resorts and has one of the highest snow Avalanche Hazard Indices of any major road in North America (Nepstad et al. 2006). Given that small-scale spatial and temporal gradients in precipitation intensity and hydrometeor type directly affect snow avalanche conditions, this paper also illustrates the potential for using a gap-filling dual-polarized X-band radar to improve the analysis and prediction of precipitation and avalanche hazard within LCC.

2. Data and methods

a. Doppler on Wheels

High-resolution radar scans from DOW6, an X-band (3.2-cm wavelength) dual-polarized Doppler weather radar developed by the CSWR (Wurman et al. 1997) and operated by students from the University of Utah, provide the cornerstone for this analysis. During IOP6, DOW6 operated near the southwest corner of the SLV at an elevation of 1508 m—about 200 m above the lowest point in the SLV (Fig. 2a). The continuous scanning strategy included plan position indicator (PPI) scans at approximately 1° intervals between 0.5° and 13.7° and range–height indicator (RHI) scans over LCC, the surrounding central Wasatch Mountains, and the eastern SLV. Although DOW6 operated from 1405 UTC 12 November to 0402 UTC 13 November
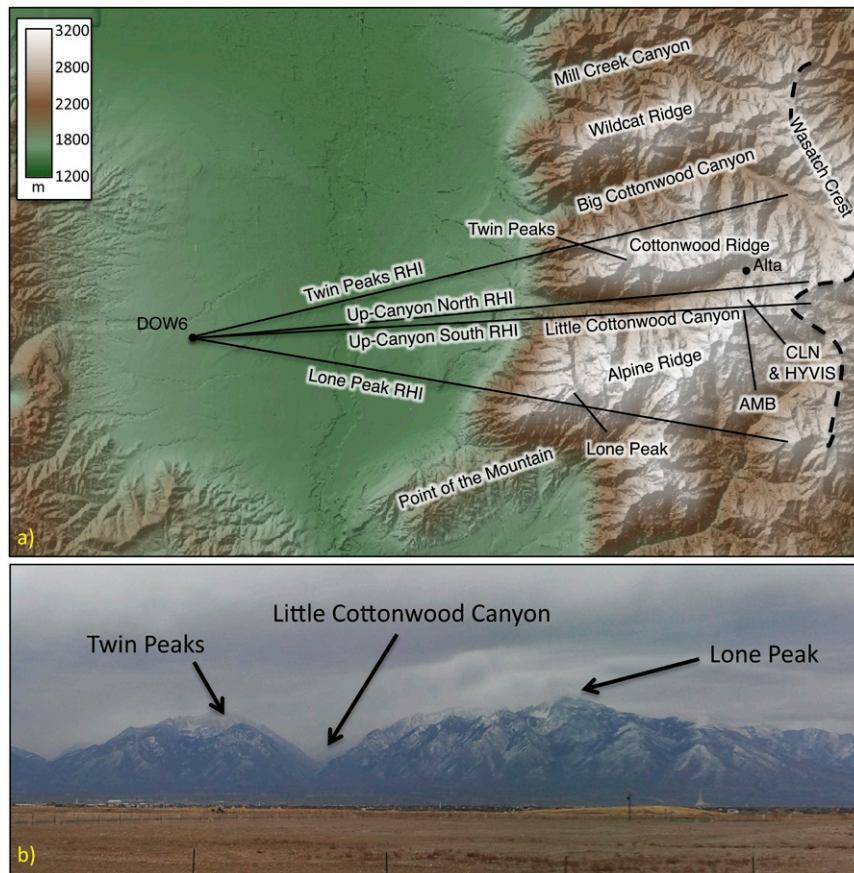
FIG. 2. (a) Topography of the central Wasatch Mountains, including locations of RHI scans in and around LCC. Dashed line denotes the hydrological divide, or Wasatch Crest. (b) View of LCC and surrounding topography from the DOW6 site.

2011, precipitation after 2130 UTC 13 November 2011 was light in LCC and is not discussed here.

Software programs Solo II and Xltrs II (Oye et al. 1995) were used initially to visualize, process, and translate the DOW6 data. Processing and quality control included the reorientation of PPI and RHI scans relative to true north, the application of a normalized coherent power (a measure of the "coherence" of the data in which noisy range gates exhibit values near zero) minimum of 0.25, and the removal of range gates exhibiting both low-velocity and high-reflectivity values as ground clutter. No corrections were made for attenuation, as attenuation rates in snow are very low (Rinehart 1997). A low bias in radar reflectivity may exist down beam of topographic features that generate partial beam blockage (James et al. 2000); however, these range gates were not removed. The maximum unambiguous range was ~48 km, and velocity unfolding was performed at a Nyquist velocity of $19.6 \, \text{m s}^{-1}$. Individual PPI and RHI scans were interpolated onto Cartesian grids with 75-m horizontal and 50-m vertical resolution, factoring in a $4/3$

Earth radius assumption and standard atmospheric refraction conditions (Rinehart 1997).

Time-mean reflectivity and velocity RHIs reflect the average reflectivity or velocity value of each range gate for the specified time period. Composite time-mean reflectivity PPIs are produced by first creating time-mean reflectivity PPIs for each scan angle between 3.2° and 13.7°, then by calculating the maximum value for each range gate between all scan angles. For both RHIs and PPIs, the averaging process eliminates range gates with undefined values or with fewer than five real values for the time period from the time-mean calculation.

The hydrometeor typing algorithm follows the work of Dolan and Rutledge (2009), which uses a fuzzy-logic approach involving horizontally polarized radar reflectivity, dual-polarization variables (e.g., differential reflectivity, specific differential phase, and correlation coefficient), and vertical temperature profiles (obtained from soundings launched from KSLC and the DOW6 site). Schneebeli et al. (2013) recently used this algorithm to examine the microphysical processes contributing to

precipitation in the Swiss Alps. The Dolan and Rutledge (2009) algorithm uses a T-matrix scattering model with seven modeled hydrometeor types (vertically aligned ice, ice crystals, aggregates, low-density graupel, high-density graupel, drizzle/light rain, and rain). Four of these hydrometeor types were identified by the algorithm during IOP6: 1) ice crystals (assumed to have diameters smaller than 1.5 mm, small axis ratios of 0.1–0.3, densities between 0.4 and 0.9 g cm^{-3}, and temperatures between $-40°$ and $-10°$C), 2) aggregates (assumed to be conglomerates of semispherical, randomly oriented ice crystals with diameters of 1–12 mm, axis ratios of 0.2–0.9, densities between 0.1 and 0.2 g cm^{-3}, and temperatures between $-15°$ and $5°$C), 3) drizzle/light rain (assumed to be small spherical droplets with diameters of 0.3–0.55 mm and temperatures above $0°$C), and 4) low-density graupel (assumed to have axis ratios of 0.5–1.25, densities between 0.25 and 0.55 g cm^{-3}, and temperatures between $-20°$ and $5°$C). The low-density graupel temperature range is a modification from the range (from $-20°$ to $-10°$C) used by Dolan and Rutledge (2009) to reflect observations of partially to fully rimed ice crystals and small graupel at higher temperatures during wintertime storms in the central Wasatch Mountains. Specific differential phase, which is dependent on axis ratio and particle concentration and is used most commonly for the detection of heavy rain, was not available for much of IOP6; therefore, the algorithm used in this paper does not include this variable.

The hydrometeor-type RHIs reflect the most frequently identified hydrometeor type for each range gate across the specified time interval, and are presented along with selected images captured by a hydrometeor videosonde (HYVIS; Murakami and Matsuo 1990) snowflake camera system, located near 2990 m at Alta Ski Area in upper LCC, for comparison. The HYVIS system takes two-dimensional photographs of snowflakes from the side as they fall through a cylindrical tube, cataloging them by time stamp. While the quality of these images is variable, the shape and size of the silhouettes allow us to subjectively classify the snow crystals. The HYVIS system was located in a sheltered grove of trees ~360 m north of the Up-Canyon South RHI scan, ~1000 m south of the Up-Canyon North RHI scan, and ~340 m north of the Alta-Collins (CLN) weather station (Fig. 2a, locations approximate). The hydrometeor-type algorithm was run using the Up-Canyon South RHI for all time periods except 1430–1700 UTC, when the Up-Canyon South RHI was not available and the Up-Canyon North RHI was used.

b. Supplemental meteorological data

Regional-scale precipitation features were examined using lowest-tilt (0.5°) base reflectivity scans from the Salt Lake City, Utah (KMTX), National Weather Service Weather Surveillance Radar-1988 Doppler (WSR-88D), which were obtained in level II format (Crum et al. 1993) from the National Climatic Data Center (NCDC) Next Generation Weather Radar (NEXRAD) archive. KMTX is located on Promontory Point, a major peninsula of the Great Salt Lake, at 2004 m—about 500 m above the DOW6 site and about 700 m above the SLV floor (Fig. 1a). For clarity, KMTX data were smoothed using a moving-average filter with a span of 10 data points.

University of Utah students launched GRAW GPS-based upper-air soundings from the DOW6 site periodically during the event. Profiles of squared dry N_d^2 and moist N_m^2 Brunt–Väisälä frequencies were calculated from these soundings following Durran and Klemp (1982), and were smoothed using a moving-average filter with a span of 10 data points. Time–height cross sections and plan-view analyses from the Rapid Update Cycle, version 2 (RUC2; Benjamin et al. 1998), available at 13-km grid spacing, were used to assess synoptic conditions. Surface observations, including hourly liquid equivalent precipitation, were obtained from the MesoWest cooperative networks (Horel et al. 2002).

3. Event overview

During the event sampled by IOP6, a progressive upper-level short-wave trough moved across northern Utah, with the accompanying surface cold front passing KSLC at 1940 UTC 12 November and entering LCC at 2030 UTC 12 November. We divide IOP6 into three stages: prefrontal, frontal (rather than transitional given the existence of a well-defined surface cold front), and postfrontal. Due to the gradual progression of the cold front across the study area, we have defined a later onset of the frontal and postfrontal stages in LCC compared to KSLC. The lengthy prefrontal stage (0900–1940 UTC 12 November at KSLC and 0900–2030 UTC 12 November at LCC) featured a weakly stratified atmosphere with a dry (i.e., relative humidity <80%) subcloud layer below ~750 hPa (Fig. 3). Over the SLV, winds veered with height from southerly or southeasterly near the surface (see later sounding and surface analysis figures) to west-southwesterly near crest level (~700 hPa). With the passage of the shallow cold front (frontal stage; 1940–2100 UTC 12 November at KSLC and 2030–2130 UTC 12 November at LCC) the flow below crest level shifted to northwesterly, whereas westerly flow persisted above crest level. During the postfrontal stage (2100–0400 UTC 12–13 November at KSLC and 2130–0400 UTC 12–13 November at LCC), westerly to northwesterly flow prevailed and contained a transient mesoscale snowband
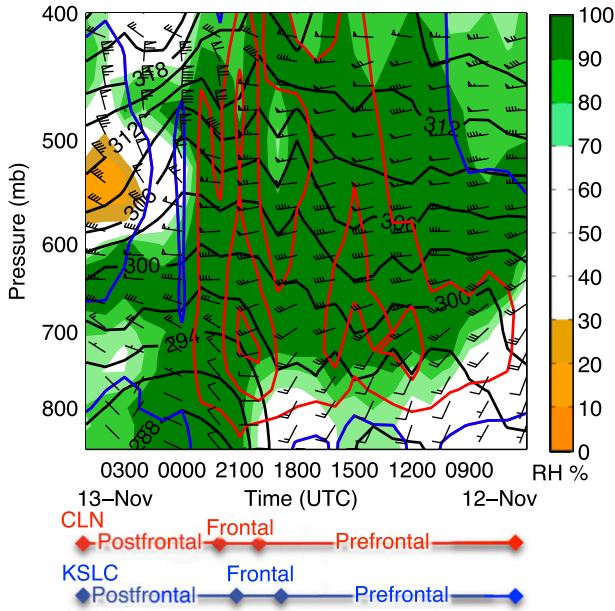
FIG. 3. RUC2 KSLC time–height section of θ_e (black contours every 3 K), pressure vertical velocity [contours every 1 Pa s^{-1} with red (blue) indicating upward (downward) motion], wind (full and half barbs denote 5 and 2.5 m s^{-1}, respectively), and relative humidity (%; shaded following scale at right). Times of prefrontal, frontal, and postfrontal stages for CLN (red) and KSLC (blue) are annotated at the bottom.

that affected KSLC, but weakened before reaching LCC, where scattered convective snow showers were observed. The event concluded at ~0400 UTC 13 November as drier air moved into northern Utah.

The event produced 6 in. (15 cm) of snow and 0.75 in. (1.9 cm) of liquid equivalent at CLN in upper LCC and 0.19 in. (0.47 cm, in the form of rain or wet snow) of liquid equivalent at KSLC in the SLV (see Figs. 1a and 2a for locations). Although CLN recorded measurable precipitation during each of the three storm stages, KSLC did not record any during the prefrontal and frontal stages, with all the measureable precipitation falling during the passage of the mesoscale snowband in the postfrontal stage (Fig. 4). The remainder of this paper describes the structure and evolution of precipitation as observed by DOW6 during the prefrontal and frontal storm stages, with an emphasis on LCC. We elect to not present the postfrontal stage due to the weak precipitation rates and the lack of variation in precipitation structure in and around LCC, opting instead to focus on the richer comparison between the prefrontal and frontal stages.

4. Orographic precipitation structures during the prefrontal stage

DOW6 operations for IOP6 commenced at 1405 UTC 12 November, near the midpoint of the prefrontal stage.
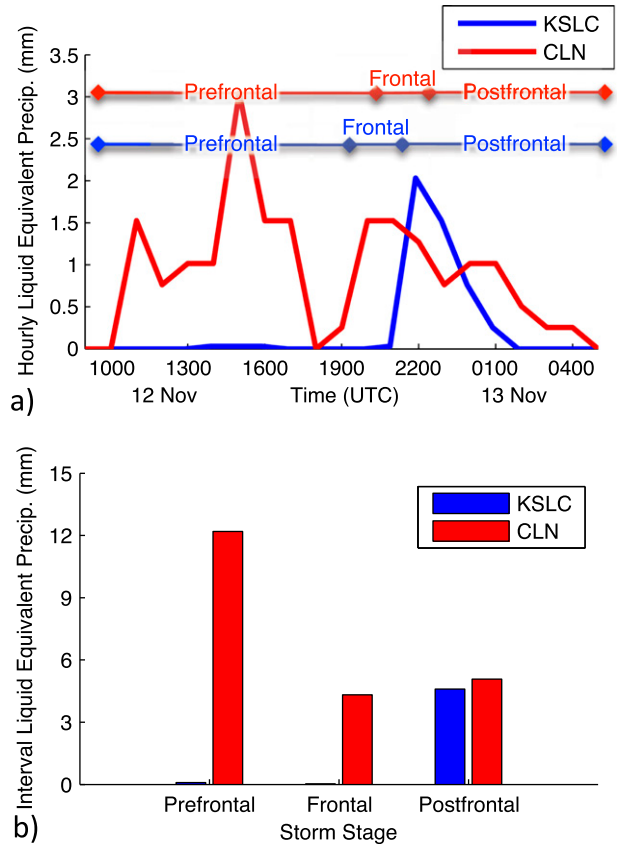

FIG. 4. (a) Hourly accumulated liquid equivalent precipitation (mm) at KSLC and CLN with major stages annotated. (b) Accumulated liquid equivalent precipitation (mm) for each storm stage at KSLC and CLN.

At 1500 UTC 12 November, the 500-hPa trough axis and vorticity maximum were over Idaho, with the surface cold front and leading edge of the accompanying 700-hPa baroclinic zone positioned over northwest Utah [Figs. 5a,b (surface front not shown)]. The prefrontal atmosphere over the SLV was stably stratified with a near moist-adiabatic lapse rate from the surface to ~700 hPa and a dry subcloud layer with dewpoint depressions as large as 9.5°C below 630 hPa (Figs. 6a,c). Winds veered from southeasterly at the surface to southwesterly near crest level (~700 hPa) and westerly at 600 hPa (Fig. 6c). This veering wind profile likely reflects weak prefrontal warm advection combined with the channeling of flow in the SLV, the latter consistent with the unsaturated conditions and relatively large squared Brunt–Väisälä frequency (i.e., N_d^2) below crest level (~700 hPa; Fig. 6b). Although it is challenging to effectively utilize the Froude number ($U/N_d H$), with observed data in regions of highly irregular terrain (e.g., Reinecke and Durran 2008), it does help indicate the tendency for air to move either around or over topographic
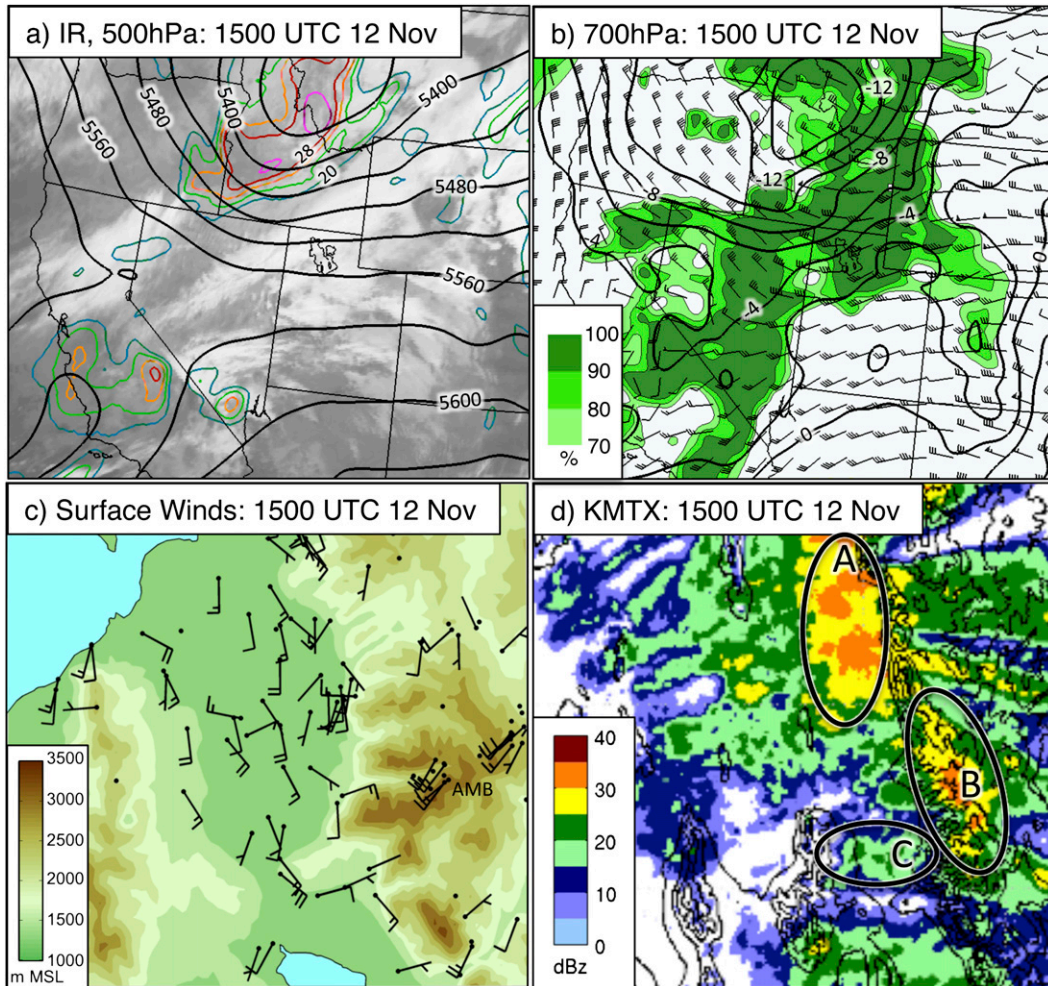
FIG. 5. Environmental conditions at 1500 UTC 12 Nov: (a) RUC2 500-hPa geopotential height (black contours every 60 m) and absolute vorticity (colored contours every $4 \times 10^{-5}\,s^{-1}$) overlaid on infrared satellite imagery; (b) RUC2 700-hPa temperature (black contours every 2°C), wind (full and half barbs denote 5 and 2.5 m s^{-1}, respectively), and relative humidity (%; shaded following scale at bottom left); (c) MesoWest surface wind observations [wind barbs as in (b)] and terrain elevation (m; shaded following scale at lower left); and (d) KMTX lowest-elevation angle (0.5°) base reflectivity (shaded following scale at lower left).

obstacles. In this case, using the mean N_d (=1.4 × $10^{-2}\,s^{-1}$), mean wind speed U (=12.4 m s^{-1}),[1] and a barrier height of 1800 m yields a mean Froude number of ~0.5 below 775 mb, further supporting the likelihood of low-level flow channeling.

During this period, the KMTX radar showed persistent quasi-stationary echoes in three areas (e.g., Fig. 5d). The first is in the lowlands upstream of the northern Wasatch Mountains where there was an area of windward precipitation enhancement (hereafter the windward

precipitation region; labeled A), as frequently occurs during large-scale southwesterly flow (e.g., Cox et al. 2005). The second is over the central Wasatch Mountains east of the SLV, including upper LCC, where there was a barrier-scale precipitation maximum near the Wasatch Crest (hereafter the barrier-scale precipitation maximum; labeled B). The third is over the southern SLV where a west–east-oriented band of higher reflectivity (15–25 dBZ) extended from the Oquirrh Mountains into the central Wasatch Mountains near LCC (hereafter the cross-valley band; labeled C). The barrier-scale precipitation maximum and the cross-valley band are also present in DOW6 PPI scans (composite time mean shown later). Although a prominent feature on KMTX and DOW6 PPI scans, the cross-valley band

---

[1] Based on the total wind because the cross-barrier direction cannot be determined unambiguously given the terrain three-dimensionality.

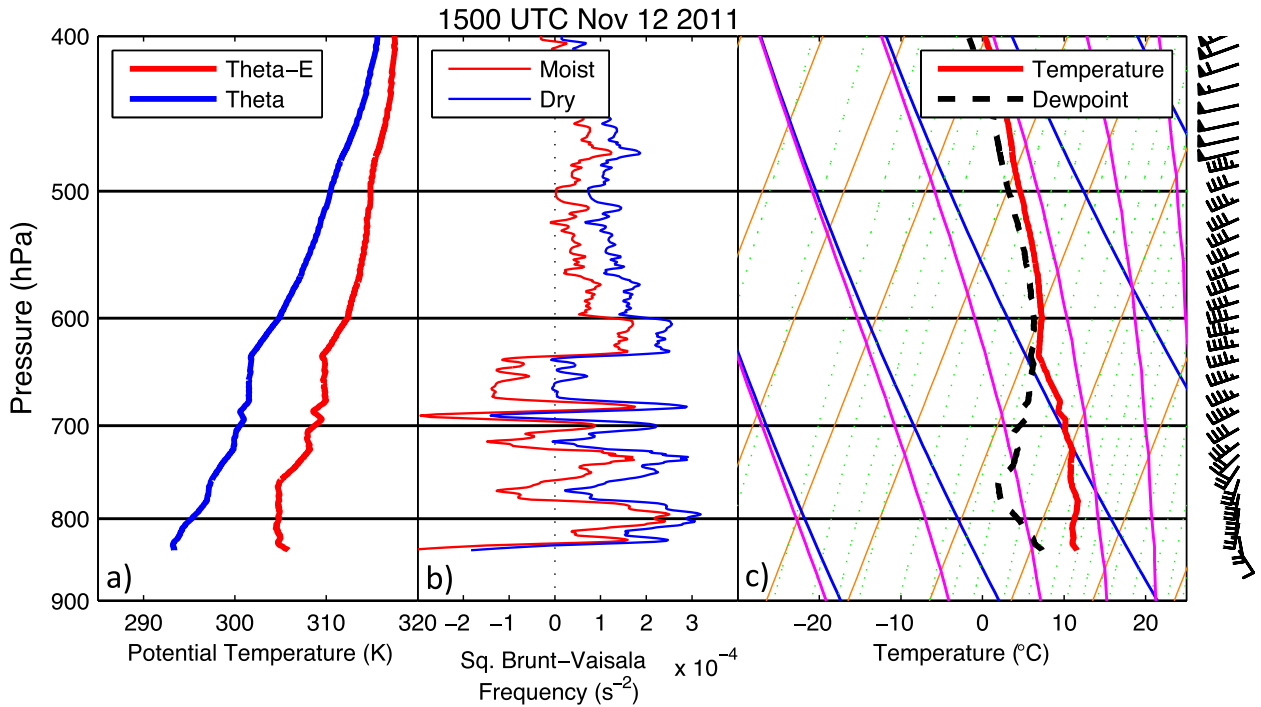FIG. 6. Upper-air observations at 1500 UTC 12 Nov at DOW6 site: (a) θ and θ_e, (b) N_d^2 and N_m^2, and (c) skew T–log p diagram [temperature, dewpoint, and wind barbs (full and half barbs denote 5 and 2.5 m s^{-1}, respectively)].

produced little measurable precipitation in the SLV due to sublimation below cloud base [the lowest-elevation tilt of the KMTX radar is centered 1500 m or more above the SLV floor (Wood et al. 2003)]. Given the west-southwesterly flow, the lack of windward precipitation enhancement upstream of the central Wasatch Mountains may reflect shadowing effects of the Stansbury and Oquirrh Mountains (see Fig. 1a for locations), but the mechanisms behind the formation and maintenance of the cross-valley band are less clear.

The Up-Canyon North RHI scan (see inset for location) from 1543 UTC 12 November illustrates the wavelike radar reflectivity structure that formed over the

SLV and LCC by the cross-valley band and barrier-scale precipitation maximum (Fig. 7). High radar reflectivities associated with the cross-valley band descend from west–east across the SLV and then ascend, broaden, and strengthen within the wavelike barrier-scale precipitation maximum over the middle of LCC before sloping downward over upper LCC. During this period CLN recorded light precipitation (1.5–3 mm h^{-1} liquid equivalent; Fig. 4a) and upper LCC was visually obscured (not shown).

Time-mean reflectivity RHIs for 1430–1700 UTC 12 November (Figs. 8a–c) show a similar structure over the Cottonwood and Alpine Ridges to the north and south
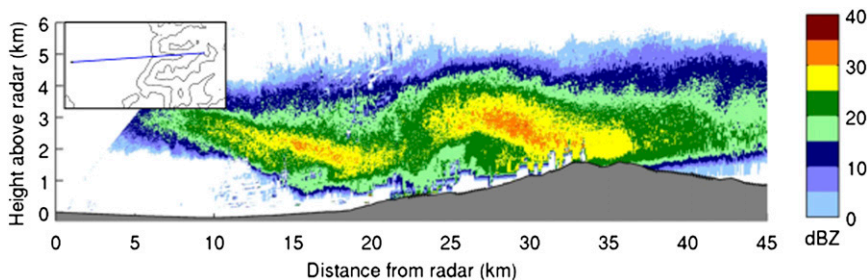

FIG. 7. Radar reflectivity Up-Canyon North RHI scan (dBZ; shaded following scale at right) for 1543 UTC 12 Nov. Inset shows the location of the RHI scan over the topography in and around LCC.
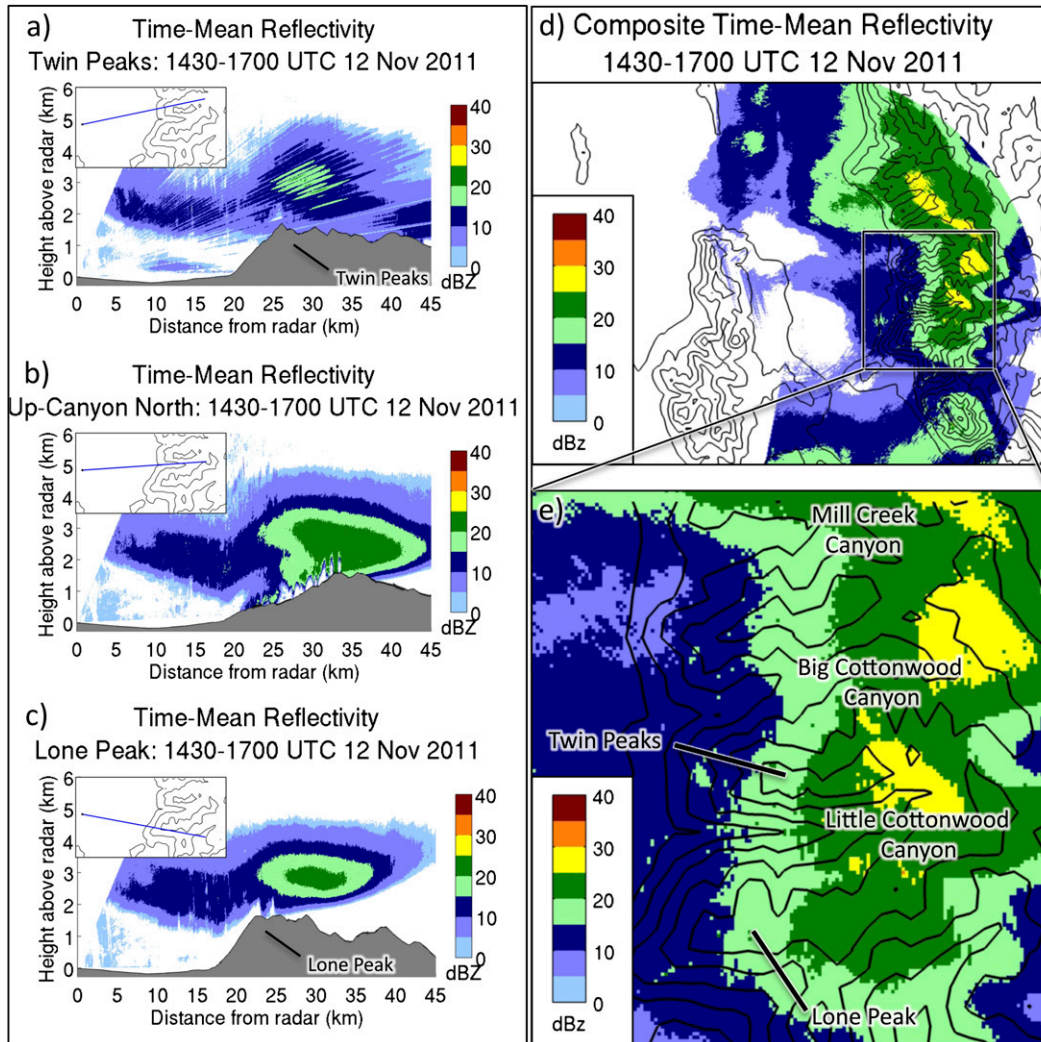
FIG. 8. Time-mean radar reflectivity (dBZ; shaded following scale at right) for 1430–1700 UTC 12 Nov. Insets show the location of each RHI scan over the topography in and around LCC. Shown are RHIs for (a) Twin Peaks, (b) Up-Canyon North, and (c) Lone Peak. Time-mean composite radar reflectivity for 1430–1700 UTC 12 Nov (dBZ; shaded following the scale at bottom left) for (d) the SLV region and (e) the central Wasatch Mountains.

of LCC, respectively.[2] Note the eastward displacement (downstream relative to the midlevel flow) of the reflectivity maximum relative to Twin Peaks and Lone Peak, despite the fact that these peaks form the windward face of the central Wasatch Mountains, rising ~2000 m above the SLV. The composite time-mean reflectivity PPI for 1430–1700 UTC 12 November also shows this displacement (Fig. 8d), with the barrier-scale

reflectivity maximum located along the Wasatch Crest and east (downstream relative to the midlevel flow) of the initial windward peaks.

The Up-Canyon North time-mean Doppler velocity RHI for 1430–1700 UTC 12 November (Fig. 9a) shows a shallow layer of inbound radial velocities over the SLV, consistent with the southeasterly surface flow (Fig. 5c). This is surmounted by a layer of strong Doppler velocity shear that, like the radar reflectivity maximum, slopes upward over lower and middle LCC, reaching a maximum height ~26 km from the radar before sloping downward over upper LCC (cf. Figs. 9a and 8b). The Lone Peak time-mean Doppler velocity RHI for 1430–1700 UTC 12 November shows similar characteristics

---

[2] A data collection error affected some of the RHI scans over Twin Peaks, causing the stripes of missing or erroneous data evident in Fig. 8a and later in Fig. 12a, but the overall structure of the radar reflectivity was preserved.
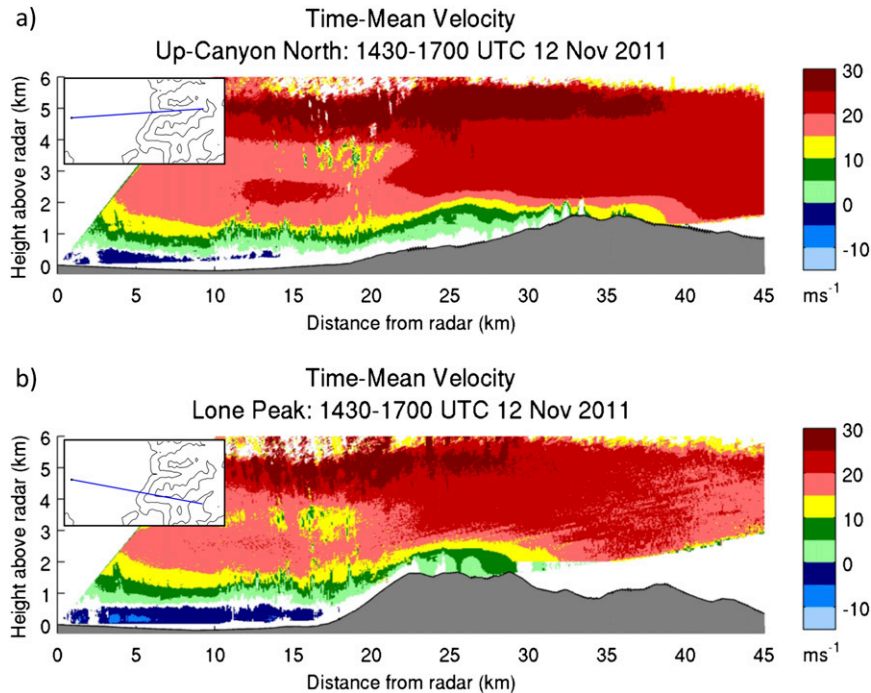
FIG. 9. Time-mean Doppler velocity (m s^{-1}; shaded following scale at right, positive values denote flow away from radar) for 1430–1700 UTC 12 Nov. Insets show the locations of each RHI scan over the topography in and around LCC. RHIs for (a) Up-Canyon North and (b) Lone Peak are shown.

(Fig. 9b), but with a steeper slope over the western face of Lone Peak leading to a maximum height that is about ~500 m higher than is found over LCC (cf. Figs. 9a,b). MesoWest observations from Mount Baldy (AMB; 3373 m; see Fig. 2a for location) and surrounding sites show 20–30 m s^{-1} south-southwesterly flow penetrating across the Alpine Ridge south of LCC during this period (Fig. 5c). This is a stronger flow with a more southerly orientation than is found at a comparable elevation

(~650 hPa) in the 1500 UTC 12 November sounding taken over the SLV (Fig. 6). Thus, beneath the sloping shear layer and inferred layer of cross-barrier flow that generated the barrier-scale precipitation maximum, south-southwesterly flow was able to surmount the Alpine Ridge and descend over LCC. A similar structure in Twin Peak RHIs (not shown) suggests a shallow wave-like flow across the ridge–canyon corrugations of the central Wasatch Mountains. Strong directional shear
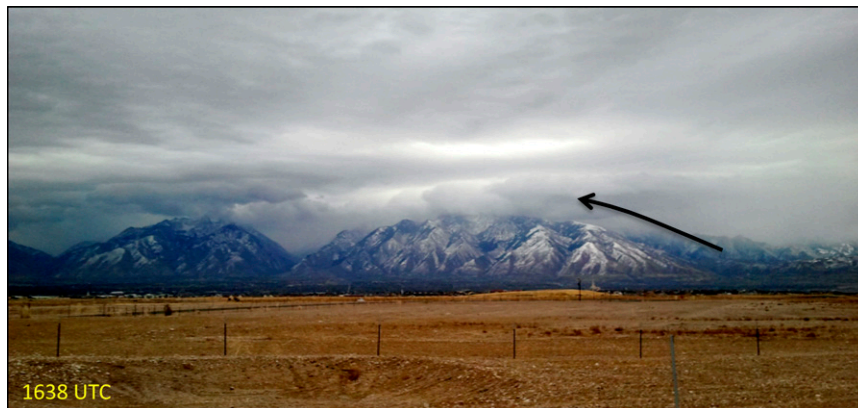

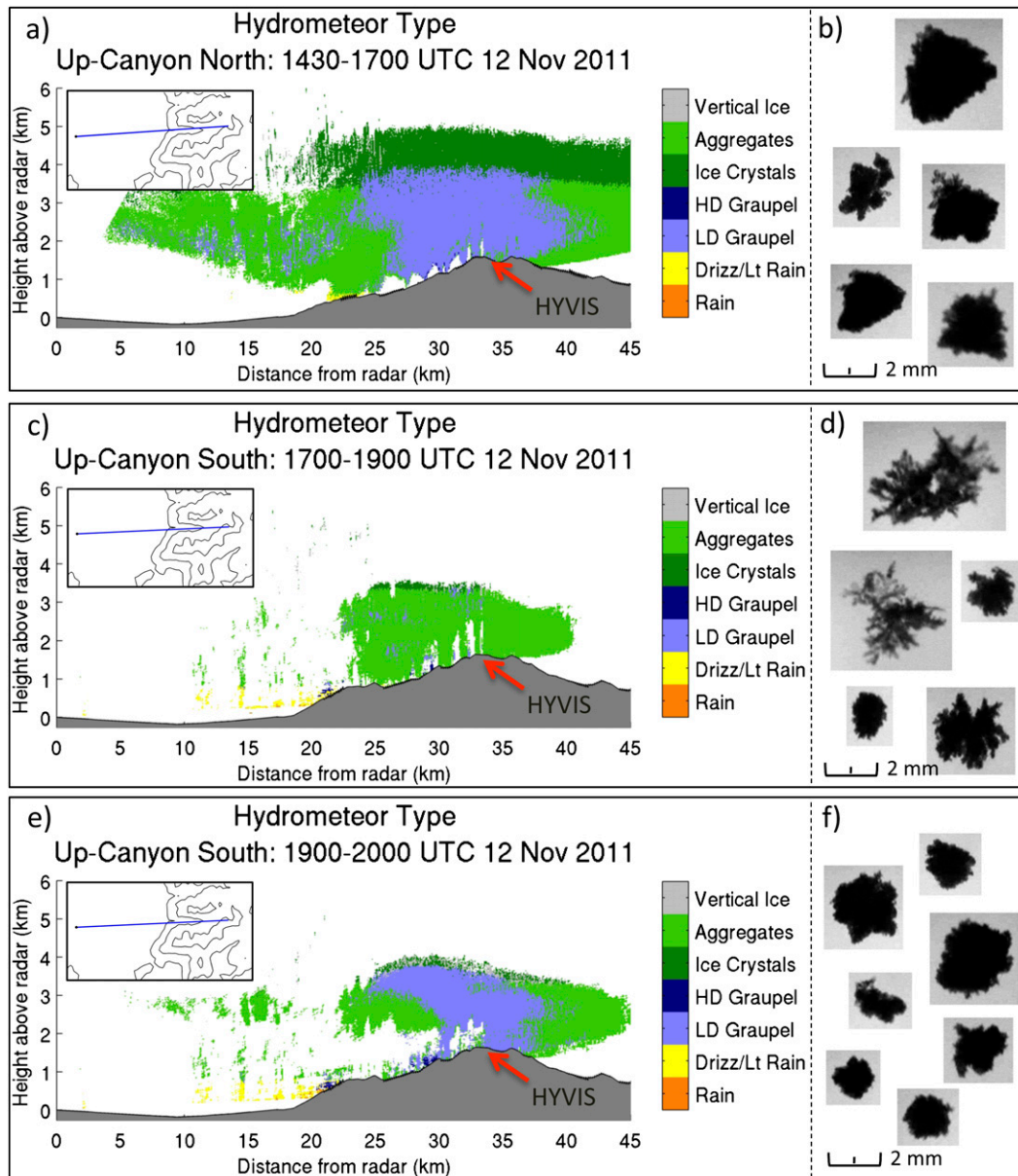FIG. 10. Photo of prefrontal clouds in and around LCC taken from the DOW6 site at 1638 UTC 12 Nov.

FIG. 11. Predominant hydrometeor type (shading following the legend at right where HD and LD refers to high density and low density and drizz/lt rain refers to drizzle or light rain) and images of snowflakes observed in upper LCC during the same time period. Insets show the location of each RHI scan over the topography in and around LCC. Shown are (a),(b) Up-Canyon North, 1430–1700 UTC 12 Nov; (c),(d) Up-Canyon South, 1700–1900 UTC 12 Nov; and (e),(f) Up-Canyon South, 1900–2000 UTC 12 Nov.

(e.g., Fig. 6) may have limited the upward penetration of terrain-induced gravity waves (e.g., Doyle and Jiang 2006; Garvert et al. 2007), resulting in the shallow wavelike flow. The 1638 UTC 12 November photograph from the DOW6 site shows the shallow orographic clouds generated by this flow over Lone Peak and Twin Peaks (Fig. 10). Careful inspection of the composite time-mean reflectivity PPI shows a tendency for higher

reflectivities to extend westward over the Wildcat, Cottonwood, and Alpine Ridges and retract eastward over Mill Creek Canyon, Big Cottonwood Canyon, and LCC (Fig. 8e). Garvert et al. (2007) describe similar ridge–canyon effects over the Cascade Mountains.

Up-Canyon North hydrometeor-type RHIs for 1430–1700 UTC 12 November identify a region of low-density graupel (25–40 km from the radar) above mid- to upper
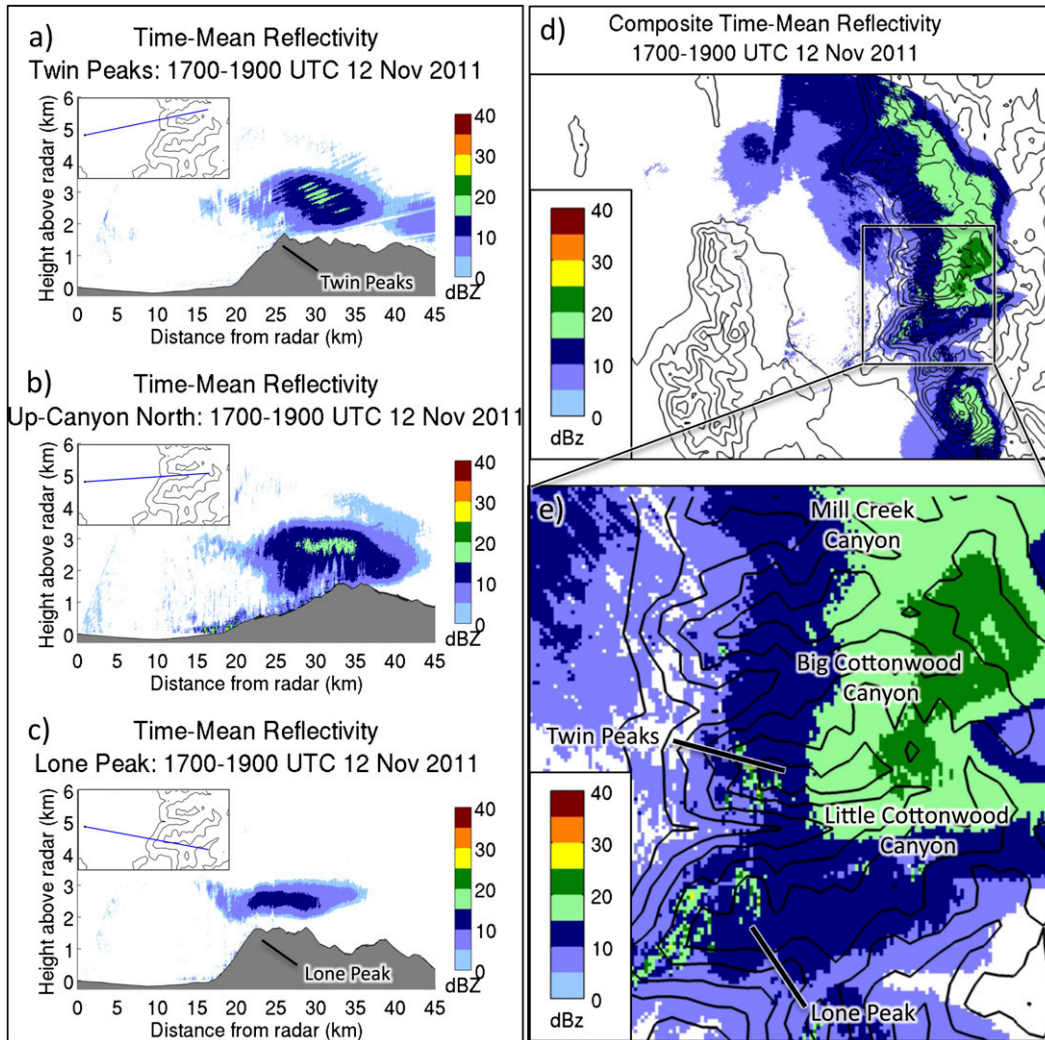
FIG. 12. As in Fig. 8, but for 1700–1900 UTC 12 Nov.

LCC (Fig. 11a) that is roughly collocated with the wavelike reflectivity maximum noted in radar reflectivity RHIs (Figs. 7 and 8a–c). Ice crystals are shown in the higher reaches of the precipitating cloud, while aggregates are shown west (upstream) and east (downstream) of the region of low-density graupel. The HYVIS camera documented images of hydrometeors in upper LCC during this period that, due to their shape, size, and the temperature within the cloud layer, are most likely rimed crystals and small graupel (Fig. 11b). The presence of graupel and rimed crystals likely reflects higher cloud liquid water concentrations and stronger wavelike ascent into the barrier-scale precipitation maximum.

Between 1700 and 1900 UTC 12 November, the windward precipitation band upstream of the northern Wasatch Mountains dissipated with the approach of the cold front (not shown). Over and around the SLV, the cross-valley band dissipated, the barrier-scale precipitation maximum persisted in a somewhat weakened state (Fig. 12), and precipitation rates at CLN ebbed (Fig. 4). Although the time-mean Doppler velocity RHIs have gaps in coverage over the valley due to the lack of radar returns throughout much of this period, the velocity signatures above mid- to upper LCC and Lone Peak show that the Doppler velocity shear layer is flatter, no longer exhibiting a wavelike shape over LCC (cf. Figs. 9 and 13). In addition, the hydrometeor-type RHI shows aggregates to be the predominant hydrometeor type over the upper canyon, which is consistent with the observed ice crystal types (Figs. 11c,d) and reflects a transition from the graupel and heavily rimed crystals observed earlier.

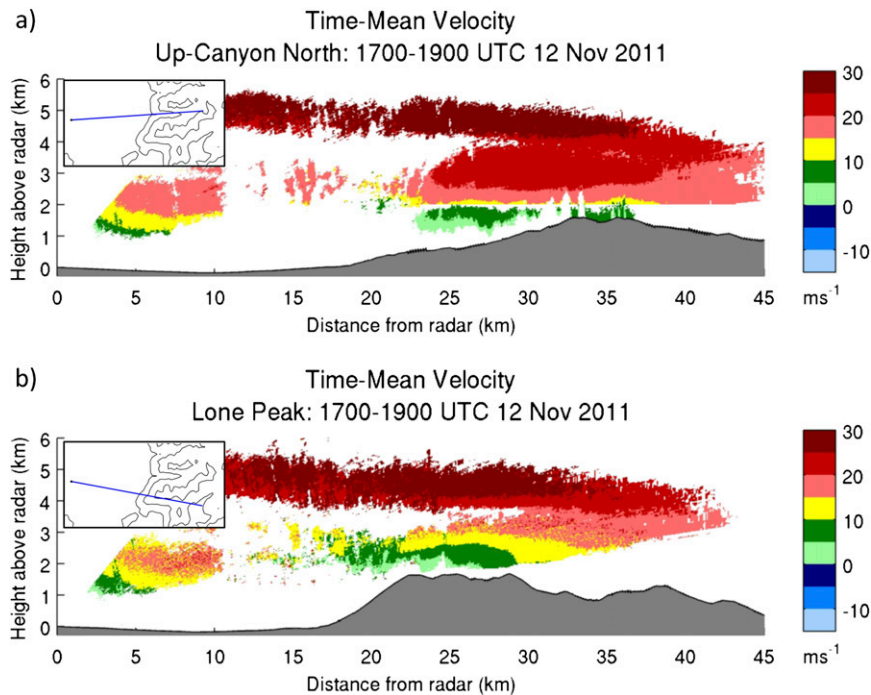These changes suggest a shift in the dominant precipitation processes compared to earlier in IOP6 when

FIG. 13. As in Fig. 9, but for 1700–1900 UTC 12 Nov.

the precipitation rates, radar reflectivities, riming, and graupel content were all greater. This is broadly consistent with weaker large-scale ascent and lower surface–725-hPa relative humidities found in the RUC2 analysis at 1800 UTC 12 November (Fig. 3) and the inferred weakening of the wavelike structure in radar reflectivity and Doppler velocity shear from 1700 to 1900 UTC. However, the wavelike reflectivity feature and area of low-density graupel redeveloped (not shown) over upper LCC (Figs. 11e,f) from 1900 to 2000 UTC before the cold front entered LCC. These contrasts and variations suggest that the increase in vertical motion during periods of stronger wavelike undulations across the central Wasatch increased the available cloud liquid water and resultant riming over LCC.

5. Precipitation structures during the frontal stage

At 2000 UTC 12 November, the surface cold front was moving through the SLV (wind shift visible in Fig. 14c) with the 500-hPa trough axis and 700-hPa baroclinic zone just upstream (Figs. 14a,b). Just after frontal passage, at 2030 UTC 12 November, a sounding launched from the DOW6 site showed shallow northwesterly flow with two apparent frontal stable layers between 825 and 775 hPa (Fig. 15).

The shallow cold front, which was distorted by the Oquirrh and Wasatch Mountains as it progressed into the SLV, was much weaker at upper elevations (Fig. 16a; front analyzed at lower elevations where it was well defined). For example, the frontal passage produced a dramatic wind shift (from south to north) and large temperature decline (8°C) from 1930 to 2030 UTC at KSLC, whereas only a gradual wind shift (from south-southwest to west-southwest) and temperature fall (1.4°C) occurred at AMB from 2000 to 2300 UTC. A band of radar reflectivity ~30 km wide (hereafter the frontal band) accompanied the cold front, and its presence defines the frontal stages at KSLC (1940–2100 UTC 12 November) and LCC (2025–2130 UTC 12 November). As the frontal band moved into the SLV, it was strongly modulated by the terrain with enhancement on the western slopes of the Oquirrh Mountains, shadowing over the western SLV, and enhancement again over the western slopes of the Wasatch Mountains (Fig. 16a). By 2030 UTC 12 November (Fig. 16b), the front had penetrated to the south end of the SLV and was draped across lower LCC. Enhancement of the frontal band continued over the Oquirrh and Wasatch Mountains while the western SLV remained shadowed. By 2100 UTC 12 November (Fig. 16c), the cold front was south of the SLV and LCC and precipitation was confined to very near to and over the Wasatch Mountains. At the same time, a broader area of postfrontal precipitation stalled over the northern end of the SLV.
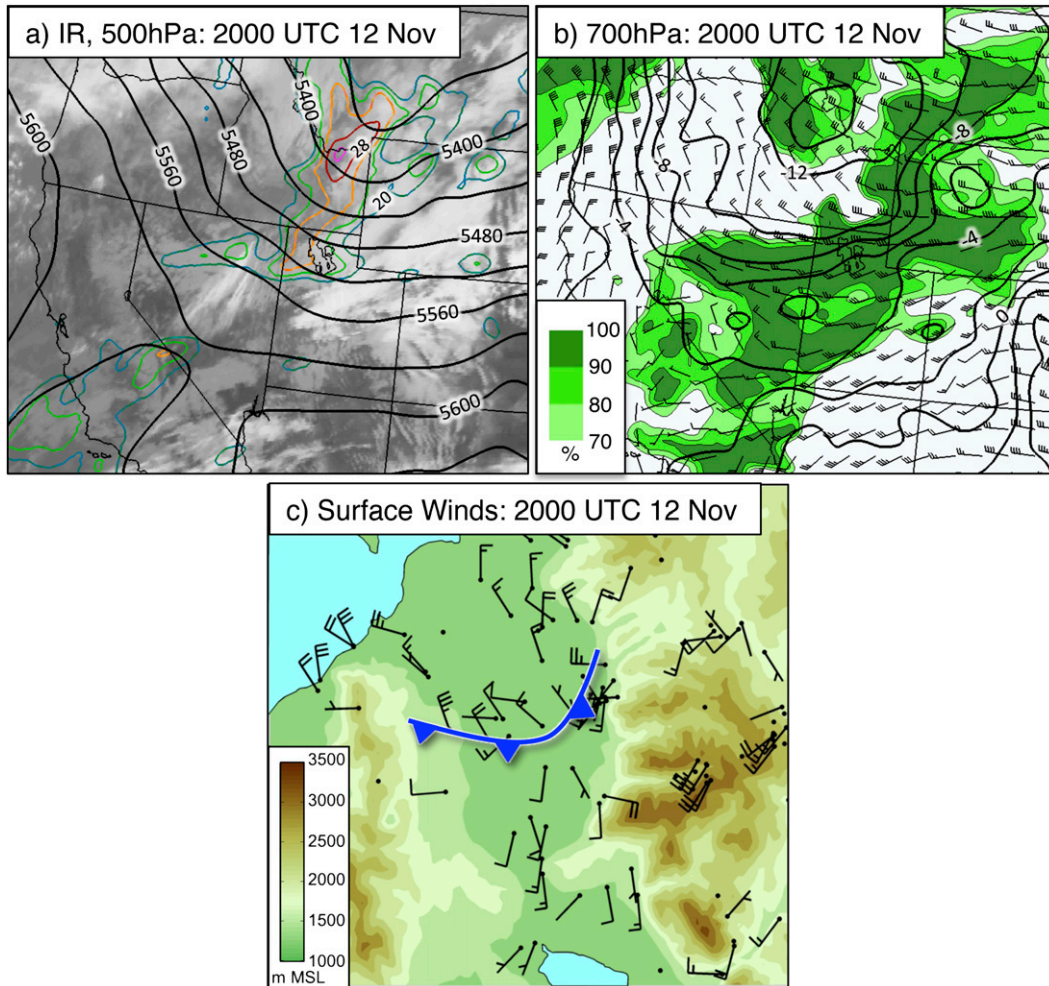
FIG. 14. (a),(b) As in Figs. 5a,b, but at 2000 UTC 12 Nov. (c) As in Fig. 5c, but for manual surface-front analysis (heavy blue line) and at 2000 UTC 12 Nov.

Up-Canyon South radar reflectivity RHIs between 2026 and 2052 UTC 12 November document the precipitation structure in and around LCC during frontal passage (Fig. 17). As the canyon is oriented roughly west–east and the cold front was oriented southwest–northeast, these RHIs cut obliquely through the front. At 2026 UTC 12 November, the RHI slices through the frontal band ~10 km from the radar, where there is an elevated region of 20–30 dBZ reflectivities (Fig. 17a, labeled area 1). Lower reflectivities below this maximum suggest the sublimation of hydrometeors in the subsaturated air below crest level (Fig. 15), and a photograph taken at 1957 UTC 12 November from the DOW6 site (looking toward the west face of the central Wasatch Mountains; Fig. 18) shows the sublimation of precipitation behind the fractus cloud at the leading edge of the cold front. By 2032 UTC 12 November, the frontal band had moved across the Cottonwood Ridge and

into LCC, increasing midcanyon radar reflectivities (Fig. 17b, labeled area 2). This area of high reflectivities became shallower by 2039 UTC 12 November (Fig. 17c, labeled area 3) and gradually became concentrated in the lower canyon (Fig. 17d, labeled area 4). After passage of the frontal band, radar reflectivities diminished significantly and became quite shallow in and around LCC. In the lower canyon, however, a small reflectivity maximum averaging 15–20 dBZ persisted until ~2130 UTC 12 November (not shown).

Time-mean reflectivity RHIs for 2025–2100 UTC 12 November show a region of frontal precipitation within LCC, with the strongest reflectivities over the midcanyon (Fig. 19b). Time-mean reflectivities over the Cottonwood and Alpine Ridges to the north and south did not reach a comparable depth or intensity as those within the canyon during this period (Figs. 19a,c). These marked contrasts are also visible in the composite
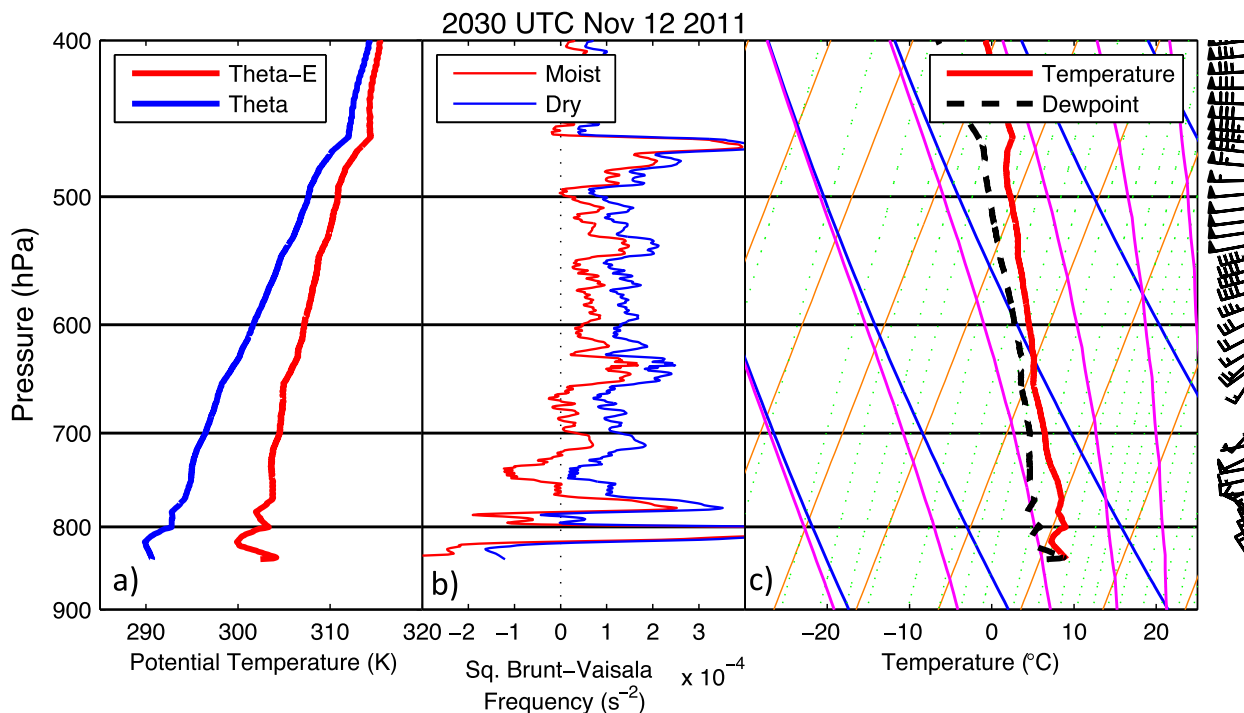
FIG. 15. As in Fig. 6, but for 2030 UTC 12 Nov.

time-mean reflectivity PPI scan for the period (Figs. 19d,e), which shows the highest radar reflectivities within lower LCC as well as over the north- to northwest-facing walls of lower Mill Creek Canyon, Big Cottonwood Canyon, and LCC. Reflectivities were lower at high elevations along the Wildcat, Cottonwood, and Alpine Ridges, implying that the storm during this period was relatively shallow with localized, northwesterly upslope flow immediately behind the front creating orographic enhancement along the north- to northwest-facing canyon walls.

As the cold front progressed through LCC, the hydrometeor-type RHI for 2025–2100 UTC 12 November (Fig. 20a) shows a layer of low-density graupel extending over LCC and the SLV with a shallow layer of aggregates at low levels over the SLV. The vigorous vertical motion often associated with surface-based cold fronts (e.g., Sanders 1955; Carbone 1982; Shapiro 1984) likely resulted in riming, and observations of what is most likely graupel and heavily rimed crystals over upper LCC (Fig. 20b) confirm the hydrometeor classification at higher elevations. There is no way to ascertain the actual hydrometeor types over the SLV at this time because of sublimation and a lack of snow crystal identification observations in the SLV; however, it is unlikely that a precipitating cloud would be composed of such a broad layer of aggregates below a layer of graupel. This suggests either a misclassification of the

predominant hydrometeor type over the SLV by the Dolan and Rutledge (2009) algorithm or a shift in the actual hydrometeor types over the SLV during passage of the frontal precipitation band due to rapidly changing atmospheric conditions. Houze and Medina (2005) found a similar misclassification between large aggregates and graupel using the hydrometeor typing algorithm of Vivekanandan et al. (1999).

6. Discussion

The above analysis illustrates the finescale spatiotemporal variability of orographic precipitation observed in the central Wasatch Mountains of northern Utah during IOP6 (12–13 November 2011) of SCHUSS. Although we caution against viewing IOP6 as a "typical" event because the characteristics of winter storms over the central Wasatch Mountains vary and feature a wide range of precipitation processes, rates, and distributions (e.g., Dunn 1983; Steenburgh 2003, 2014), we believe the event provides useful insight into the finescale nature of precipitation features in areas of complex three-dimensional topography and the challenges confronting operational meteorologists and forecast consumers during winter storms in mountainous regions.

During IOP6, persistent quasi-stationary radar reflectivity features were observed in and around LCC and the SLV during the prefrontal stage, including
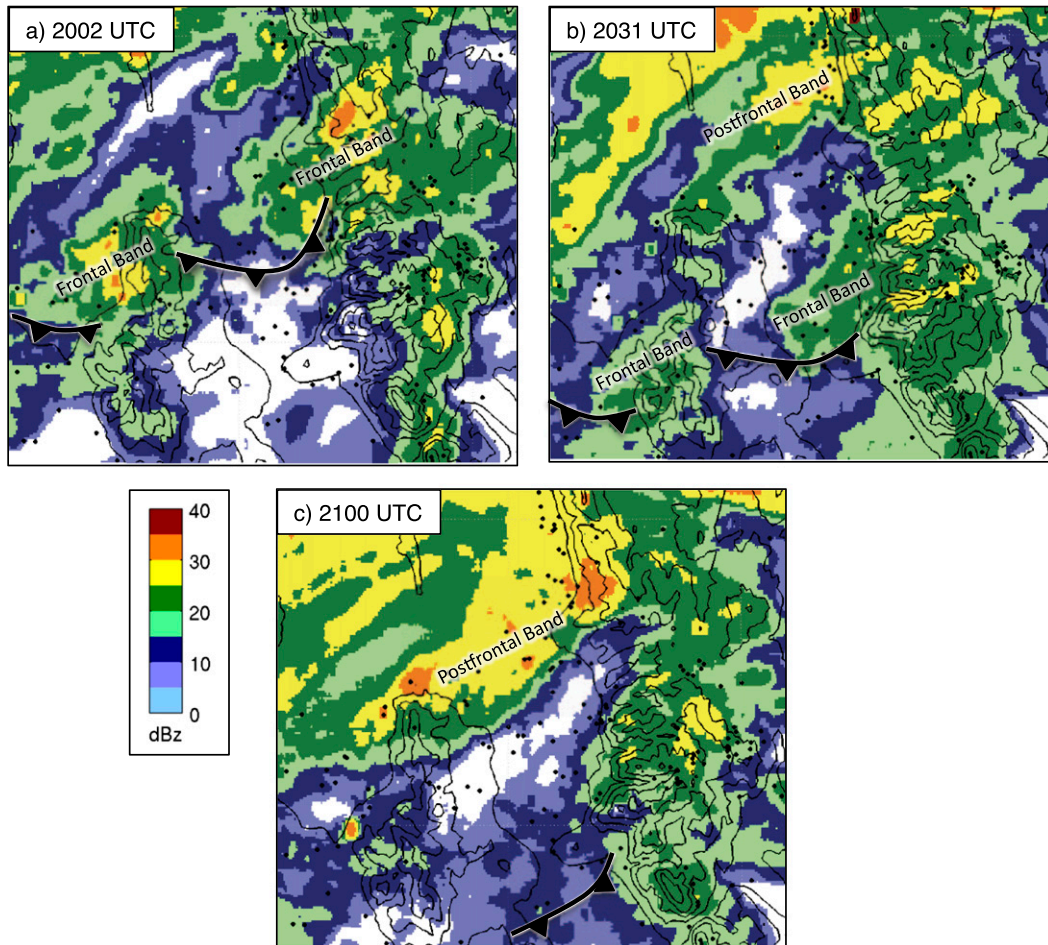
FIG. 16. KMTX lowest-elevation angle (0.5°) base reflectivity (shaded following scale at bottom left) and manual surface-front analysis (heavy black line) at (a) 2002 UTC 12 Nov, (b) 2031 UTC 12 Nov, and (c) 2100 UTC 12 Nov. Black dots mark the locations of MesoWest stations used in the analysis of the surface-front boundary.

1) a barrier-scale precipitation maximum over the Wasatch Crest and east, or downstream, of the high windward peaks (relative to the midlevel flow); 2) protrusions of higher reflectivity over the transverse ridges flanking LCC; and 3) a cross-valley band of precipitation that extended from the Oquirrh Mountains across the SLV and into the central Wasatch Mountains. RHI scans through these features revealed a wavelike radar reflectivity structure that sloped downward from west to east across the SLV (cross-valley band), while high reflectivities associated with the barrier-scale precipitation maximum ascended, broadened, and strengthened over middle LCC before descending over upper LCC and the Wasatch Crest. Beneath the midlevel, cross-barrier westerly flow, strong southwesterly crest-level winds appeared to generate shallow wavelike flow across the west–east-oriented ridge–canyon corrugations of the

central Wasatch Mountains (summarized conceptually in Fig. 21) and protrusions of higher reflectivity over the ridges flanking LCC. Graupel and heavily rimed crystals were identified by the hydrometeor-type algorithm and were observed in upper LCC during periods when the barrier-scale precipitation maximum featured a robust wavelike appearance suggestive of enhanced barrier-scale ascent. In contrast, aggregates were identified by the hydrometeor-type algorithm and were observed in upper LCC during periods when the barrier-scale precipitation maximum was weaker and lacked a wavelike structure.

During the frontal stage, the terrain flanking the SLV modulated the cold-frontal precipitation band, producing shadowing over the western SLV to the lee (east) of the Oquirrh Mountains and enhancement over the eastern SLV windward of the central Wasatch
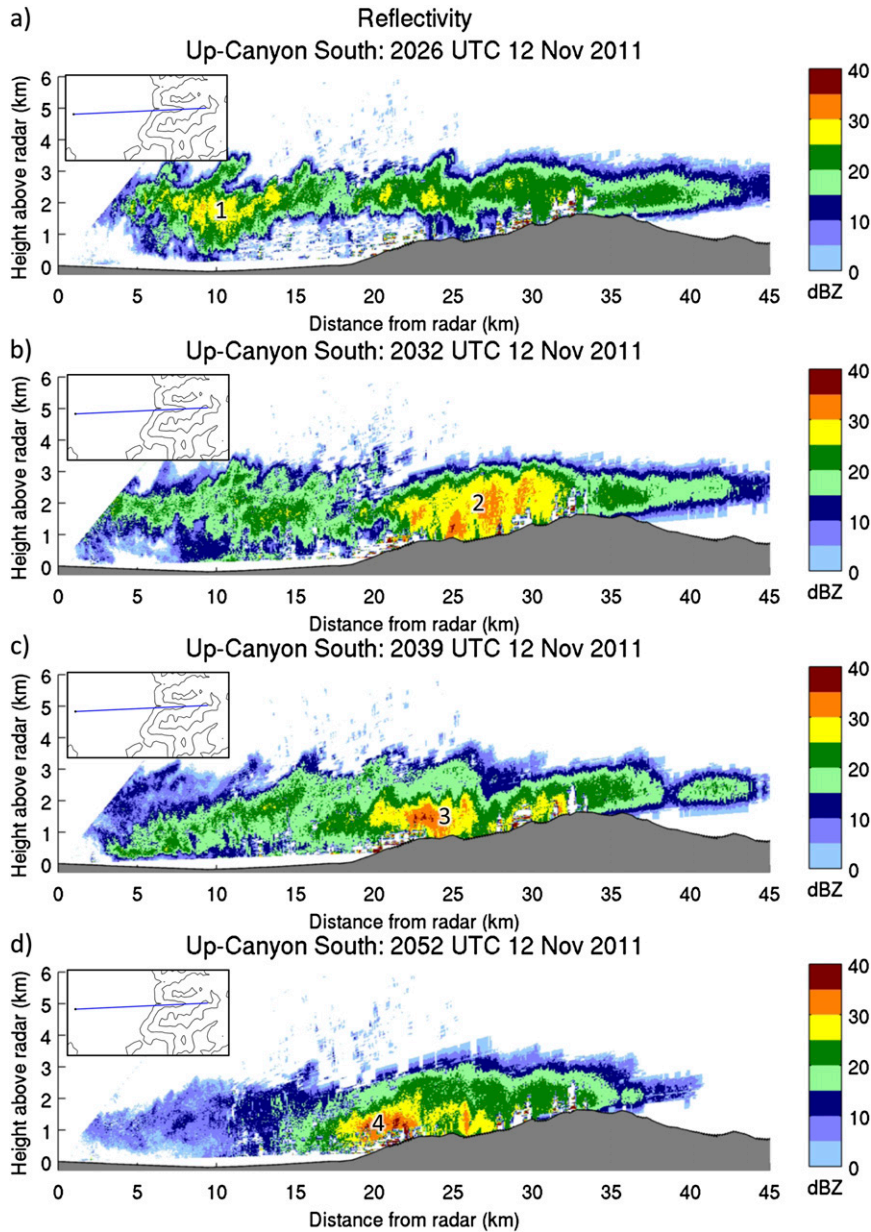
FIG. 17. Up-Canyon South radar reflectivity RHI scans (dBZ; shaded following scale at right) at (a) 2026 UTC 12 Nov, (b) 2032 UTC 12 Nov, (c) 2039 UTC 12 Nov, and (d) 2052 UTC 12 Nov. Insets show the location of the RHI scan over the topography in and around LCC.

Mountains. During and following cold-frontal passage, the strongest radar reflectivities were found over lower LCC and the north- to northwest-facing canyon wall. Similar reflectivity maxima were also observed over the north- to northwest-facing walls of Mill Creek and Big Cottonwood Canyons. In contrast, reflectivities were lower in upper LCC and at high elevations along the Wildcat, Cottonwood, and Alpine Ridges. This pattern appeared to be the result of the frontal dynamics, the

low elevation of the frontal capping inversion (below crest level), and the shallow, postfrontal, northwesterly upslope flow over the north- to northwest-facing canyon walls.

The resulting spatial contrasts in reflectivity patterns between the prefrontal and frontal stages are striking. During the prefrontal stage, the composite time-mean reflectivity PPI for 1430–1700 UTC 12 November shows high radar reflectivities in upper LCC and along the

FIG. 18. Photograph of surface-based cold front looking northeast from the DOW6 site. Note the fractus cloud above the leading edge of the cold front, and the sublimation behind it.

Wasatch Crest eastward (downstream relative to the midlevel flow) of the high windward peaks, with slight protrusions of higher radar reflectivities along the transverse ridges. In contrast, the composite time-mean reflectivity PPI for the frontal stage (2025–2100 UTC 12 November) shows a near reversal of this spatial pattern with the highest radar reflectivities found in lower LCC and at midlevels along the north- to northwest-facing walls of lower LCC and neighboring canyons.

Meteorologists frequently use climatological precipitation–altitude relationships, such as the one presented in Fig. 1b, to make inferences about the distribution of precipitation during winter storms over complex terrain (Meyers and Steenburgh 2013). This includes the interpretation of radar imagery for inferring precipitation rates or nowcasting, and the downscaling or confidence assessment of the numerical forecast guidance available at grid spacings ranging from ~1 to 25 km. For an event like IOP6, however, such an approach is fraught with problems. During the prefrontal stage, it would have resulted in an overprediction of precipitation along the western abutments of the Alpine and Cottonwood Ridges and possibly also in lower LCC where low-level sublimation reduced precipitation rates. During the frontal stage, the strongest radar reflectivities were found within lower to middle LCC and over the north- to northwest-facing walls of lower LCC and neighboring canyons, whereas climatology would suggest an increase in precipitation with elevation, resulting in the heaviest precipitation in upper LCC and along the Alpine and Cottonwood Ridges. Although there is some potential to predict such variations with cloud-permitting or cloud-resolving

modeling systems, current real-time modeling systems run at 4-km grid spacing struggle with event-to-event predictions on these finescales (e.g., Minder et al. 2008).

LCC provides an excellent example of how these analysis and forecast uncertainties ultimately affect public safety and economic activities in heavily used mountain areas. SR-210 follows the north side of LCC from the SLV to the terminus of LCC and is traveled by an average of more than 7000 vehicles each day during winter. Fifty snow avalanche paths bisect the highway, adjoining roads, and parking lots, with steep road grades and high snowfall rates frequently leading to hazardous driving conditions and bumper-to-bumper traffic during winter storms (Fig. 22). An average of 33 avalanches hit SR-210 each year, and the combination of frequent large avalanches and the volume and speed of traffic gives the highway one of the highest Avalanche Hazard Indices of any major road in North America (Nepstad et al. 2006; Steenburgh 2014). Avalanche forecasters for SR-210 generally close the highway when the avalanche hazard is high and attempt to trigger avalanches artificially using artillery. Based on data from the 1991/92 ski season, the estimated revenue loss for ski resorts in upper LCC during the closure of SR-210 for avalanche hazard is $1.4 million day^{-1} [$2.3 million day^{-1} in 2013 dollars (Blattenberger and Fowles 1995)].

Substantial potential exists to use a gap-filling radar, possibly an X-band system positioned at a location similar to that used in this study, to improve weather analysis and forecasting, avalanche control, and winter road maintenance in LCC. The avalanche hazard during a storm is greatly affected by the intensity and amount of new precipitation, as well as by the temporal and spatial
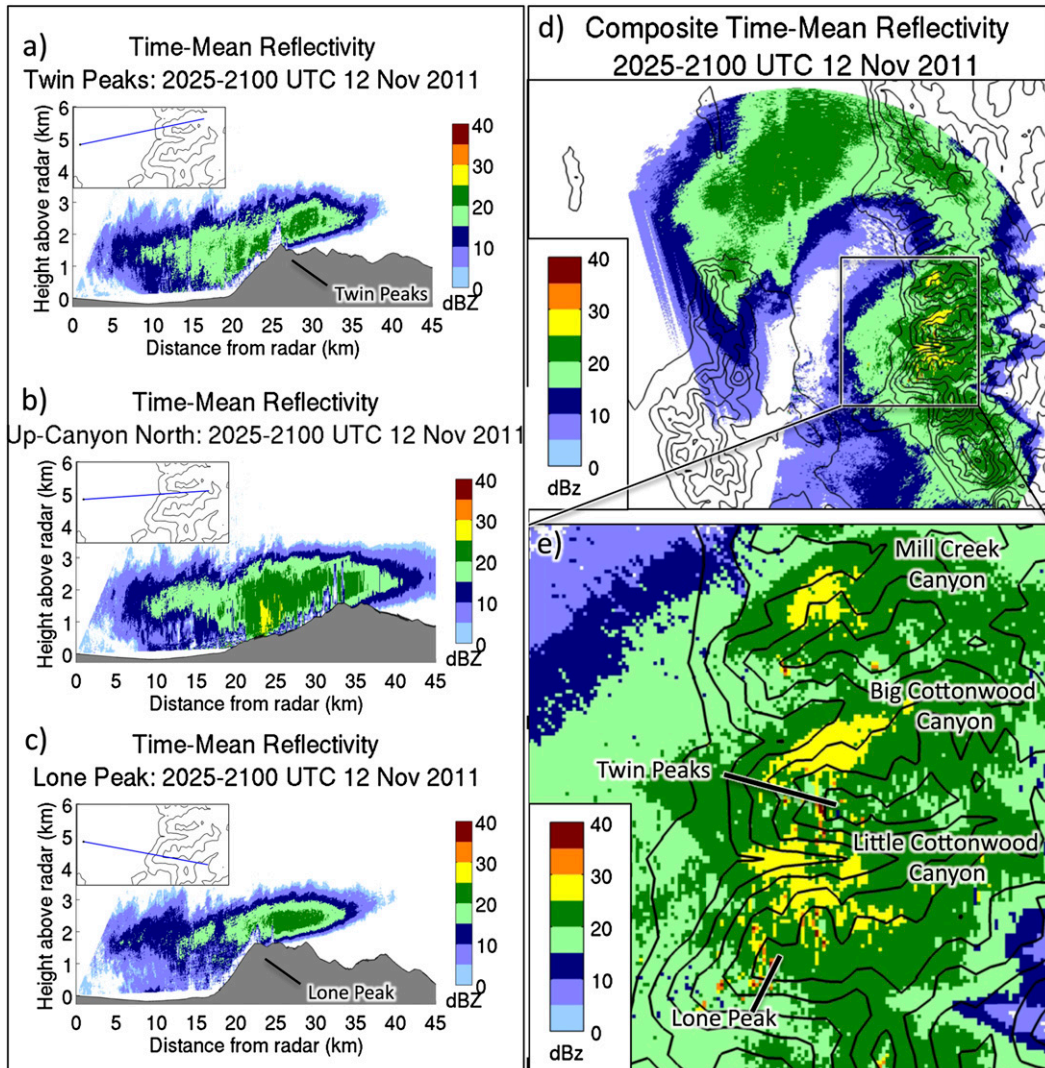
FIG. 19. As in Fig. 8, but for 2025–2100 UTC 12 Nov.

patterns of snow crystal. These storm characteristics can vary significantly within LCC, yet avalanche forecasters currently rely on hourly precipitation and wind observations collected primarily in upper LCC, as well as visual evidence of avalanche activity and crystal type, to evaluate changes in avalanche hazard during storms. The KMTX radar, however, is minimally useful during this process due to poor resolution (horizontal and vertical) and beam blockage. For example, the centroid of the lowest-elevation tilt of the KMTX radar clips the Cottonwood Ridge, resulting in ~50% blockage over LCC assuming a standard index of refraction (Wood et al. 2003). The shallow nature of orographic storms within the central Wasatch Mountains often results in overshooting or limited beam filling and coverage at low levels within LCC is nonexistent. A polarimetric gap-filling X-band radar would allow for the improved observation of precipitation features and estimates of precipitation rates along SR-210 and the starting zones of major avalanche paths, including the midcanyon White Pine and Little Pine avalanche paths (see Fig. 22), which are considered the most problematic (Nepstad et al. 2006; Steenburgh 2014). The ability to visualize precipitation intensity along SR-210 in real time, as would be possible with a gap-filling X-band radar, would greatly facilitate the decision-making process for avalanche forecasters. Although work is needed to test and improve classification algorithms, the application of hydrometeor typing in real time during storms might also prove useful for avalanche hazard assessment. The utility of X-band radar to fill gaps in radar coverage over mountainous terrain has been explored in the
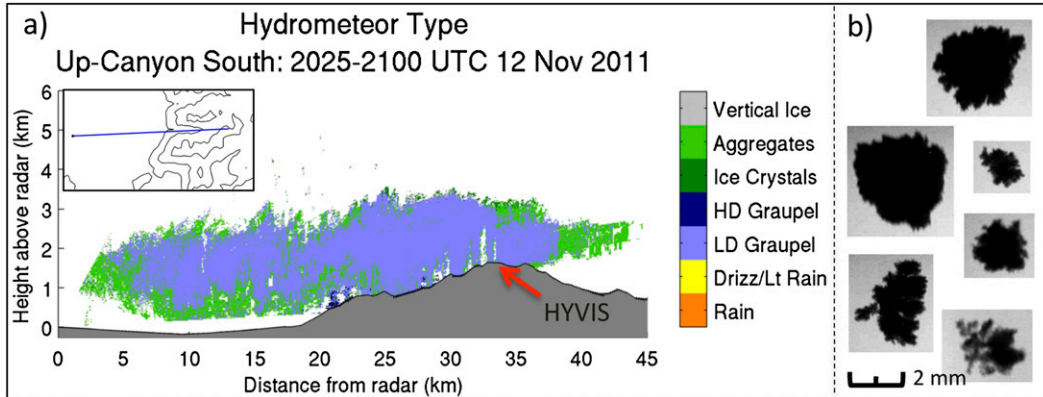
FIG. 20. As in Fig. 11, but for Up-Canyon South and for 2025–2100 UTC 12 Nov.

European Alps, where networks of X-band radars are currently being installed (e.g., Allegretti et al. 2012), and has been considered in mountainous regions within the United States (e.g., Gourley et al. 2009). In northern Utah, such a radar could be sited to also provide weather surveillance in other high-traffic-volume canyons within the central Wasatch (e.g., SR-190 in Big Cottonwood and Interstate Highway 80 in Parleys Canyon), as well as the SLV.

7. Conclusions

This paper has examined the finescale structure of a winter storm in the central Wasatch Mountains of northern Utah, with emphasis on Little Cottonwood Canyon (LCC). Significant spatiotemporal variations in storm structure occurred during the prefrontal and frontal storm stages. These small-scale variations pose a challenge for operational forecasters and forecast consumers in mountainous regions and are often not well analyzed or anticipated using conventional NEXRAD, existing operational modeling systems, or forecast techniques that employ climatological precipitation–altitude relationships. In addition, the development of numerical forecast models capable of resolving such finescale features is in its infancy, with large errors noted during individual storms in other mountainous regions (e.g., Minder et al. 2008). Significant potential exists to improve the analysis and nowcasting of precipitation within LCC and the surrounding central Wasatch Mountains using a polarimetric gap-filling X-band radar of the type utilized here. Such a system would enable improved estimates of precipitation rates and hydrometeor types along the canyon highway and within the starting zones of major avalanche paths for the benefit of avalanche control work, winter highway maintenance, and the local economy of upper LCC. Further work is needed to evaluate the economic viability of such a radar
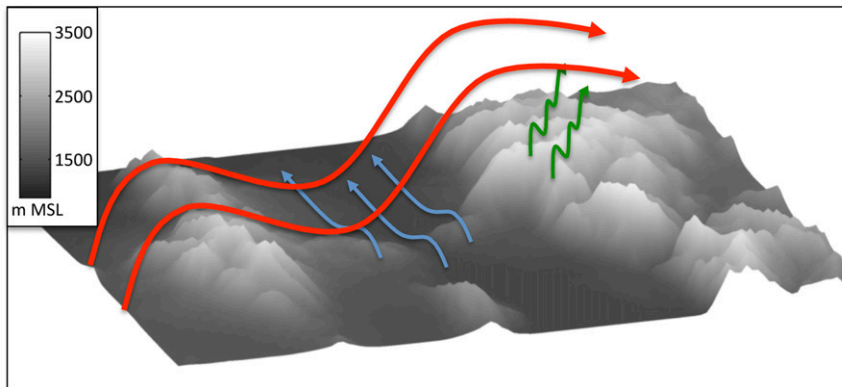

FIG. 21. Three-dimensional idealized schematic diagram of wind flow in and around the SLV for 1430–1700 UTC 12 Nov.
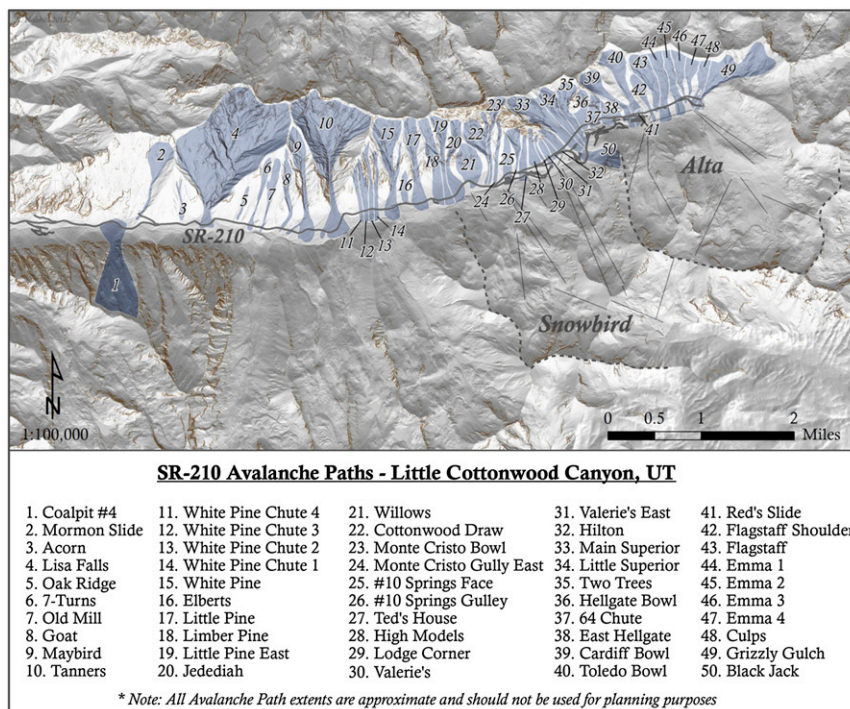
FIG. 22. Major avalanche paths affecting SR-210 in LCC. [From Steenburgh (2014). Courtesy of Utah Department of Transportation/Adam Naisbitt.]

and the fidelity of X-band estimates of precipitation rates and hydrometeor types.

REFERENCES

Allegretti, M., S. Bertoldo, A. Prato, C. Lucianaz, O. Rorato, R. Notarpietro, and M. Gabella, 2012: X-band mini radar for observing and monitoring rainfall events. *Atmos. Climate Sci.,* **2,** 290–297, doi:10.4236/acs.2012.23026.

Anders, A. M., G. H. Roe, D. R. Durran, and J. R. Minder, 2007: Small-scale spatial gradients in climatological precipitation on the Olympic Peninsula. *J. Hydrometeor.,* **8,** 1068–1081, doi:10.1175/JHM610.1.

Beck, J., and O. Bousquet, 2013: Using gap-filling radars in mountainous regions to complement a national radar network: Improvements in multiple-Doppler wind syntheses. *J. Appl. Meteor. Climatol.,* **52,** 1836–1850, doi:10.1175/JAMC-D-12-0187.1.

Benjamin, S. G., J. M. Brown, K. J. Brundage, B. E. Schwartz, T. G. Smirnova, T. L. Smith, and L. L. Morone, 1998: RUC-2—The Rapid Update Cycle version 2. NWS Tech. Procedures Bull. 448, 18 pp. [Available online at http://www.nws.noaa.gov/om/tpb/448.pdf.]

Blattenberger, G., and R. Fowles, 1995: Road closure to mitigate avalanche danger: A case study for Little Cottonwood Canyon. *Int. J. Forecasting,* **11,** 159–174, doi:10.1016/0169-2070(94)02008-D.

Bond, N. A., B. F. Smull, M. T. Stoelinga, C. P. Woods, and A. Haase, 2005: Evolution of a cold front encountering steep quasi-2D terrain: Coordinated aircraft observations on 8–9 December 2001 during IMPROVE-2. *J. Atmos. Sci.,* **62,** 3559–3579, doi:10.1175/JAS3553.1.

Bousquet, O., and B. F. Smull, 2003: Airflow and precipitation fields within deep alpine valleys observed by airborne Doppler radar. *J. Appl. Meteor.,* **42,** 1497–1513, doi:10.1175/1520-0450(2003)042<1497:AAPFWD>2.0.CO;2.

Braun, S. A., R. A. Houze Jr., and B. F. Smull, 1997: Airborne dual-Doppler observations of an intense frontal system approaching the Pacific Northwest coast. *Mon. Wea. Rev.,* **125,** 3131–3156, doi:10.1175/1520-0493(1997)125<3131:ADDOOA>2.0.CO;2.

Browning, K. A., F. F. Hill, and C. W. Pardoe, 1974: Structure and mechanism of precipitation and the effect of orography in a wintertime warm sector. *Quart. J. Roy. Meteor. Soc.,* **100,** 309–330, doi:10.1002/qj.49710042505.

Bruintjes, R. T., T. L. Clark, and W. D. Hall, 1994: Interactions between topographic airflow and cloud/precipitation development during the passage of a winter storm in Arizona. *J. Atmos. Sci.,* **51,** 48–67, doi:10.1175/1520-0469(1994)051<0048:IBTAAC>2.0.CO;2.

Caraceña, F., R. A. Maddox, L. R. Hoxit, and C. F. Chappell, 1979: Mesoanalysis of the Big Thompson storm. *Mon. Wea. Rev.,* **107,** 1–17, doi:10.1175/1520-0493(1979)107<0001:MOTBTS>2.0.CO;2.

Carbone, R. E., 1982: A severe frontal rainband. Part I: Stormwide hydrodynamic structure. *J. Atmos. Sci.,* **39,** 258–279, doi:10.1175/1520-0469(1982)039<0258:ASFRPI>2.0.CO;2.

Colle, B. A., 2004: Sensitivity of orographic precipitation to changing ambient conditions and terrain geometries: An idealized modeling perspective. *J. Atmos. Sci.,* **61,** 588–606, doi:10.1175/1520-0469(2004)061<0588:SOOPTC>2.0.CO;2.

——, 2008: Two-dimensional idealized simulations of the impact of multiple windward ridges on orographic precipitation. *J. Atmos. Sci.,* **65,** 509–523, doi:10.1175/2007JAS2305.1.

——, C. F. Mass, and B. F. Smull, 1999: An observational and numerical study of a cold front interacting with the Olympic Mountains during COAST IOP5. *Mon. Wea. Rev.,* **127,** 1310–1334, doi:10.1175/1520-0493(1999)127<1310:AOANSO>2.0.CO;2.

——, B. F. Smull, and M.-J. Yang, 2002: Numerical simulations of a landfalling cold front observed during COAST: Rapid evolution and responsible mechanisms. *Mon. Wea. Rev.,* **130,** 1945–1966, doi:10.1175/1520-0493(2002)130<1945:NSOALC>2.0.CO;2.

——, J. B. Wolfe, W. J. Steenburgh, D. E. Kingsmill, J. A. W. Cox, and J. C. Shafer, 2005: High-resolution simulations and microphysical validation of an orographic precipitation event over the Wasatch Mountains during IPEX IOP3. *Mon. Wea. Rev.,* **133,** 2947–2971, doi:10.1175/MWR3017.1.

——, R. B. Smith, and D. A. Wesley, 2013: Theory, observations, and predictions of orographic precipitation. *Mountain Weather Research and Forecasting,* F. K. Chow, S. F. J. De Wekker, and B. J. Snyder, Eds., Springer, 291–344.

Cooper, W. A., and C. P. R. Saunders, 1980: Winter storms over the San Juan Mountains. Part II: Microphysical processes. *J. Appl. Meteor.,* **19,** 927–941, doi:10.1175/1520-0450(1980)019<0927:WSOTSJ>2.0.CO;2.

Cox, J. A., W. J. Steenburgh, D. E. Kingsmill, J. C. Shafer, B. A. Colle, O. Bousquet, B. F. Smull, and H. Cai, 2005: The kinematic structure of a Wasatch Mountain winter storm during IPEX IOP3. *Mon. Wea. Rev.,* **133,** 521–542, doi:10.1175/MWR-2875.1.

Crum, T. D., R. L. Alberty, and D. W. Burgess, 1993: Recording, archiving, and using WSR-88D data. *Bull. Amer. Meteor. Soc.,* **74,** 645–653, doi:10.1175/1520-0477(1993)074<0645:RAAUWD>2.0.CO;2.

Daly, C., R. P. Neilson, and D. L. Phillips, 1994: A statistical-topographic model for mapping climatological precipitation over mountainous terrain. *J. Appl. Meteor.,* **33,** 140–158, doi:10.1175/1520-0450(1994)033<0140:ASTMFM>2.0.CO;2.

Dolan, B., and S. A. Rutledge, 2009: A theory-based hydrometeor identification algorithm for X-band polarimetric radars.

J. Atmos. Oceanic Technol., **26,** 2071–2088, doi:10.1175/2009JTECHA1208.1.

Doyle, J. D., and Q. Jiang, 2006: Observations and numerical simulations of mountain waves in the presence of directional wind shear. *Quart J. Roy. Meteor. Soc.,* **132,** 1877–1905.

Dunn, L. B., 1983: Quantitative and spatial distribution of winter precipitation along Utah's Wasatch Front. NOAA Tech. Memo. NWS WR-181, 72 pp. [Available from NOAA/NWS Western Region Headquarters, Rm. 1311, 125 S. State St., Salt Lake City, UT 84138-1102.]

Durran, D. R., and J. B. Klemp, 1982: On the effects of moisture on the Brunt–Väisälä frequency. *J. Atmos. Sci.,* **39,** 2152–2158, doi:10.1175/1520-0469(1982)039<2152:OTEOMO>2.0.CO;2.

Frei, C., and C. Schär, 1998: A precipitation climatology of the Alps from high-resolution rain-gauge observations. *Int. J. Climatol.,* **18,** 873–900, doi:10.1002/(SICI)1097-0088(19980630)18:8<873::AID-JOC255>3.0.CO;2-9.

Garvert, M. F., B. A. Colle, and C. F. Mass, 2005: The 13–14 December 2001 IMPROVE-2 event. Part I: Synoptic and mesoscale evolution and comparison with a mesoscale model simulation. *J. Atmos. Sci.,* **62,** 3474–3492, doi:10.1175/JAS3549.1.

——, B. Smull, and C. F. Mass, 2007: Multiscale mountain waves influencing a major orographic precipitation event. *J. Atmos. Sci.,* **64,** 711–737, doi:10.1175/JAS3876.1.

Godart, A., S. Anquetin, E. Leblois, and J.-D. Creutin, 2011: The contribution of orographically driven banded precipitation to the rainfall climatology of the Mediterranean region. *J. Appl. Meteor. Climatol.,* **50,** 2235–2246, doi:10.1175/JAMC-D-10-05016.1.

Gourley, J. J., D. P. Jorgensen, S. Y. Matrosov, and Z. L. Flamig, 2009: Evaluation of incremental improvements to quantitative precipitation estimates in complex terrain. *J. Hydrometeor.,* **10,** 1507–1520, doi:10.1175/2009JHM1125.1.

Hill, G. E., 1978: Observations of precipitation-forced circulations in winter orographic storms. *J. Atmos. Sci.,* **35,** 1463–1472, doi:10.1175/1520-0469(1978)035<1463:OOPFCI>2.0.CO;2.

Hobbs, P. V., 1975: The nature of winter clouds and precipitation in the Cascade Mountains and their modification by artificial seeding. Part I: Natural conditions. *J. Appl. Meteor.,* **14,** 783–804, doi:10.1175/1520-0450(1975)014<0783:TNOWCA>2.0.CO;2.

Horel, J., and Coauthors, 2002: MesoWest: Cooperative mesonets in the western United States. *Bull. Amer. Meteor. Soc.,* **83,** 211–225, doi:10.1175/1520-0477(2002)083<0211:MCMITW>2.3.CO;2.

Houze, R. A., Jr., 2012: Orographic effects on precipitating clouds. *Rev. Geophys.,* **50,** 1–47, doi:10.1029/2011RG000365.

——, and S. Medina, 2005: Turbulence as a mechanism for orographic precipitation enhancement. *J. Atmos. Sci.,* **62,** 3599–3623, doi:10.1175/JAS3555.1.

——, C. N. James, and S. Medina, 2001: Radar observations of precipitation and airflow on the Mediterranean side of the Alps: Autumn 1998 and 1999. *Quart. J. Roy. Meteor. Soc.,* **127,** 2537–2558, doi:10.1002/qj.49712757804.

Ikeda, K., and Coauthors, 2010: Simulation of seasonal snowfall over Colorado. *Atmos. Res.,* **97,** 462–477, doi:10.1016/j.atmosres.2010.04.010.

James, C. N., S. R. Brodzik, H. Edmon, R. A. Houze Jr., and S. E. Yuter, 2000: Radar data processing and visualization over complex terrain. *Wea. Forecasting,* **15,** 327–338, doi:10.1175/1520-0434(2000)015<0327:RDPAVO>2.0.CO;2.

Kirshbaum, D. J., and D. R. Durran, 2005: Observations and modeling of banded orographic convection. *J. Atmos. Sci.,* **62,** 1463–1479, doi:10.1175/JAS3417.1.

——, G. H. Bryan, R. Rotunno, and D. R. Durran, 2007: The triggering of orographic rainbands by small-scale topography. *J. Atmos. Sci.,* **64,** 1530–1549, doi:10.1175/JAS3924.1.

Klimowski, B. A., and Coauthors, 1998: The 1995 Arizona Program: Toward a better understanding of winter storm precipitation development in mountainous terrain. *Bull. Amer. Meteor. Soc.,* **79,** 799–813, doi:10.1175/1520-0477(1998)079<0799: TAPTAB>2.0.CO;2.

Lin, Y.-L., S. Chiao, T.-A. Wang, M. L. Kaplan, and R. P. Weglarz, 2001: Some common ingredients for heavy orographic rainfall. *Wea. Forecasting,* **16,** 633–660, doi:10.1175/1520-0434(2001)016<0633: SCIFHO>2.0.CO;2.

Long, A. B., B. A. Campistron, and A. W. Huggins, 1990: Investigations of a winter mountain storm in Utah. Part I: Synoptic analyses, mesoscale kinematics, and water release rates. *J. Atmos. Sci.,* **47,** 1302–1322, doi:10.1175/1520-0469(1990)047<1302: IOAWMS>2.0.CO;2.

Maddox, R. A., L. R. Hoxit, C. F. Chappell, and F. Caracena, 1978: Comparison of meteorological aspects of the Big Thompson and Rapid City flash floods. *Mon. Wea. Rev.,* **106,** 375–389, doi:10.1175/1520-0493(1978)106<0375:COMAOT>2.0.CO;2.

Marwitz, J. D., 1980: Winter storms over the San Juan Mountains. Part I: Dynamical processes. *J. Appl. Meteor.,* **19,** 913–926, doi:10.1175/1520-0450(1980)019<0913:WSOTSJ>2.0.CO;2.

Medina, S., B. F. Smull, R. A. Houze Jr., and M. Steiner, 2005: Cross-barrier flow during orographic precipitation events: Results from MAP and IMPROVE. *J. Atmos. Sci.,* **62,** 3580–3598, doi:10.1175/JAS3554.1.

——, E. Sukovich, and R. A. Houze Jr., 2007: Vertical structures of precipitation in cyclones crossing the Oregon Cascades. *Mon. Wea. Rev.,* **135,** 3565–3586, doi:10.1175/MWR3470.1.

Meyers, M. P., and W. J. Steenburgh, 2013: Theory, observations, and predictions of orographic precipitation. *Mountain Weather Research and Forecasting,* F. K. Chow, S. F. J. De Wekker, and B. J. Snyder, Eds., Springer, 1–34.

Minder, J. R., D. R. Durran, H. Roe, and A. M. Anders, 2008: The climatology of small-scale orographic precipitation over the Olympic Mountains: Patterns and processes. *Quart. J. Roy. Meteor. Soc.,* **134,** 817–839, doi:10.1002/qj.258.

Molinié, G., D. Ceresetti, S. Anquetin, J. D. Creutin, and B. Boudevillain, 2012: Rainfall regime of a mountainous Mediterranean region: Statistical analysis at short time steps. *J. Appl. Meteor. Climatol.,* **51,** 429–448, doi:10.1175/ 2011JAMC2691.1.

Moreno, H. A., E. R. Vivoni, and D. J. Gochis, 2013: Limits to flood forecasting in the Colorado Front Range for two summer convection periods using radar nowcasting and a distributed hydrologic model. *J. Hydrometeor.,* **14,** 1075–1097, doi:10.1175/JHM-D-12-0129.1.

Murakami, M., and T. Matsuo, 1990: Development of the hydrometeor videosonde. *J. Atmos. Oceanic Technol.,* **7,** 613–620, doi:10.1175/1520-0426(1990)007<0613:DOTHV>2.0.CO;2.

Neiman, P. J., F. M. Ralph, A. B. White, D. E. Kingsmill, and P. O. G. Persson, 2002: The statistical relationship between upslope flow and rainfall in California's coastal mountains: Observations during CALJET. *Mon. Wea. Rev.,* **130,** 1468–1492, doi:10.1175/1520-0493(2002)130<1468: TSRBUF>2.0.CO;2.

——, ——, P. O. G. Persson, A. B. White, D. P. Jorgensen, and D. E. Kingsmill, 2004: Modification of fronts and precipitation by coastal blocking during an intense landfalling winter storm in Southern California: Observations during CALJET. *Mon.*

Wea. Rev., **132,** 242–273, doi:10.1175/1520-0493(2004)132<0242: MOFAPB>2.0.CO;2.

——, ——, G. A. Wick, J. D. Lundquist, and M. D. Dettinger, 2008: Meteorological characteristics and overland precipitation impacts of atmospheric rivers affecting the west coast of North America based on eight years of SSM/I satellite observations. *J. Hydrometeor.,* **9,** 22–47, doi:10.1175/2007JHM855.1.

Nepstad, J., R. Taylor, C. Stethem, and A. Clayton, 2006: Little Cottonwood Canyon transportation study. *Proc. 2006 Int. Snow Science Workshop,* Telluride, CO, ISSW. [Available at http://arc.lib.montana.edu/snow-science/item/1036.]

Oye, R., C. Mueller, and S. Smith, 1995: Software for radar translation, visualization, editing, and interpolation. *27th Conf. on Radar Meteorology,* Vail, CO, Amer. Meteor. Soc., 359–361.

Parsons, D. B., and P. V. Hobbs, 1983: The mesoscale and microscale structure and organization of clouds and precipitation in midlatitude cyclones. IX: Some effects of orography on rainbands. *J. Atmos. Sci.,* **40,** 1930–1949, doi:10.1175/1520-0469(1983)040<1930: TMAMSA>2.0.CO;2.

Peterson, T. C., L. O. Grant, W. R. Cotton, and D. C. Rogers, 1991: The effect of decoupled low-level flow on winter orographic clouds and precipitation in the Yampa River valley. *J. Appl. Meteor.,* **30,** 368–386, doi:10.1175/1520-0450(1991)030<0368: TEODLL>2.0.CO;2.

Rangno, A. L., 1986: How good are our conceptual models of orographic cloud seeding? *Precipitation Enhancement—A Scientific Challenge, Meteor. Monogr.,* No. 43, Amer. Meteor. Soc., 115–115, doi:10.1175/0065-9401-21.43.115.

Reinecke, P. A., and D. R. Durran, 2008: Estimating topographic blocking using a Froude number when the static stability is nonuniform. *J. Atmos. Sci.,* **65,** 1035–1048, doi:10.1175/ 2007JAS2100.1.

Reinking, R. F., J. B. Snider, and J. L. Coen, 2000: Influences of storm-embedded orographic gravity waves on cloud liquid water and precipitation. *J. Appl. Meteor.,* **39,** 733–759, doi:10.1175/1520-0450(2000)039<0733:IOSEOG>2.0.CO;2.

Reuder, J., G. O. Fagerlid, I. Barstad, and A. Sandvik, 2007: Stord Orographic Precipitation Experiment (STOPEX): An overview of phase I. *Adv. Geosci.,* **10,** 17–23, doi:10.5194/adgeo-10-17-2007.

Reynolds, D. W., and A. P. Kuciauskas, 1988: Remote and in situ observations of Sierra Nevada winter mountain clouds: Relationships between mesoscale structure, precipitation and liquid water. *J. Appl. Meteor.,* **27,** 140–156, doi:10.1175/ 1520-0450(1988)027<0140:RAISOO>2.0.CO;2.

Rinehart, R. E., 1997: *Radar for Meteorologists.* 3rd ed. Rinehart Publications, 428 pp.

Roe, G. H., 2005: Orographic precipitation. *Annu. Rev. Earth Planet. Sci.,* **33,** 645–671, doi:10.1146/annurev.earth.33.092203.122541.

Rotunno, R., and R. A. Houze, 2007: Lessons on orographic precipitation from the Mesoscale Alpine Programme. *Quart. J. Roy. Meteor. Soc.,* **133,** 811–830, doi:10.1002/qj.67.

Sanders, F., 1955: An investigation of the structure and dynamics of an intense surface frontal zone. *J. Meteor.,* **12,** 542–552, doi:10.1175/1520-0469(1955)012<0542:AIOTSA>2.0.CO;2.

Sassen, K., A. W. Huggins, A. B. Long, J. B. Snider, and R. J. Meitin, 1990: Investigations of a winter mountain storm in Utah. Part II: Mesoscale structure, supercooled liquid water development, and precipitation processes. *J. Atmos. Sci.,* **47,** 1323–1350, doi:10.1175/ 1520-0469(1990)047<1323:IOAWMS>2.0.CO;2.

Schneebeli, M., N. Dawes, M. Lehning, and A. Berne, 2013: High-resolution vertical profiles of X-band polarimetric radar observables during snowfall in the Swiss Alps. *J. Appl. Meteor. Climatol.,* **52,** 378–394, doi:10.1175/JAMC-D-12-015.1.

Sénési, S., P. Bougeault, J.-L. Chèze, P. Cosentino, and R.-M. Thepenier, 1996: The Vaison-La Romaine flash flood: Mesoscale analysis and predictability issues. *Wea. Forecasting,* **11,** 417–442, doi:10.1175/1520-0434(1996)011<0417:TVLRFF>2.0.CO;2.

Shapiro, M. A., 1984: Meteorological tower measurements of a surface cold front. *Mon. Wea. Rev.,* **112,** 1634–1639, doi:10.1175/1520-0493(1984)112<1634:MTMOAS>2.0.CO;2.

Sinclair, M. R., D. S. Wratt, R. D. Henderson, and W. R. Gray, 1997: Factors affecting the distribution and spillover of precipitation in the Southern Alps of New Zealand—A case study. *J. Appl. Meteor.,* **36,** 428–442, doi:10.1175/1520-0450(1997)036<0428:FATDAS>2.0.CO;2.

Smith, R. B., 2006: Progress on the theory of orographic precipitation. *Tectonics, Climate, and Landscape Evolution,* S. D. Willett et al., Eds., GSA Special Paper 398, Geological Society of America, 1–16.

——, Q. Jiang, M. G. Fearon, P. Tabary, M. Dorninger, J. D. Doyle, and R. Benoit, 2003: Orographic precipitation and air mass transformation: An Alpine example. *Quart. J. Roy. Meteor. Soc.,* **129,** 433–454, doi:10.1256/qj.01.212.

Steenburgh, W. J., 2003: One hundred inches in one hundred hours: Evolution of a Wasatch Mountain winter storm cycle. *Wea. Forecasting,* **18,** 1018–1036, doi:10.1175/1520-0434(2003)018<1018:OHIIOH>2.0.CO;2.

——, 2014: *Secrets of the Greatest Snow on Earth*. Utah State University Press, 244 pp.

Steiner, M., O. Bousquet, R. A. Houze Jr., B. F. Smull, and M. Mancini, 2003: Airflow within major Alpine river valleys under heavy rainfall. *Quart. J. Roy. Meteor. Soc.,* **129,** 411–431, doi:10.1256/qj.02.08.

Stoelinga, M. T., R. E. Stewart, G. Thompson, and J. M. Theriault, 2013: Microphysical processes within winter orographic cloud and precipitation systems. *Mountain Weather Research and Forecasting,* F. K. Chow, S. F. J. De Wekker, and B. J. Snyder, Eds., Springer, 345–408.

Viale, M., R. A. Houze Jr., and K. L. Rasmussen, 2013: Upstream orographic enhancement of a narrow cold-frontal rainband approaching the Andes. *Mon. Wea. Rev.,* **141,** 1708–1730, doi:10.1175/MWR-D-12-00138.1.

Vivekanandan, J., D. S. Zrnić, S. M. Ellis, R. Oye, A. V. Ryzhkov, and J. Straka, 1999: Cloud microphysics retrieval using S-band dual-polarization radar measurements. *Bull. Amer. Meteor. Soc.,* **80,** 381–388, doi:10.1175/1520-0477(1999)080<0381:CMRUSB>2.0.CO;2.

Western Regional Climate Center, cited 2013: Cooperative climatological data summaries. [Available online at http://www.wrcc.dri.edu/climatedata/climsum/.]

Westrick, K. J., C. F. Mass, and B. A. Colle, 1999: The limitations of the WSR-88D radar network for quantitative precipitation measurement over the coastal western United States. *Bull. Amer. Meteor. Soc.,* **80,** 2289–2298, doi:10.1175/1520-0477(1999)080<2289:TLOTWR>2.0.CO;2.

White, A. B., P. J. Neiman, F. M. Ralph, D. E. Kingsmill, and P. O. G. Persson, 2003: Coastal orographic rainfall processes observed by radar during the California Land-Falling Jets Experiment. *J. Hydrometeor.,* **4,** 264–282, doi:10.1175/1525-7541(2003)4<264:CORPOB>2.0.CO;2.

Wood, V. T., R. A. Brown, and S. V. Vasiloff, 2003: Improved detection using negative elevation angles for mountaintop WSR-88Ds. Part II: Simulations of the three radars covering Utah. *Wea. Forecasting,* **18,** 393–403, doi:10.1175/1520-0434(2003)18<393:IDUNEA>2.0.CO;2.

Woods, C. P., M. T. Stoelinga, J. D. Locatelli, and P. V. Hobbs, 2005: Microphysical processes and synergistic interaction between frontal and orographic forcing of precipitation during the 13 December 2001 IMPROVE-2 event over the Oregon Cascades. *J. Atmos. Sci.,* **62,** 3493–3519, doi:10.1175/JAS3550.1.

Wurman, J., J. Straka, E. Rasmussen, M. Randall, and A. Zahrai, 1997: Design and deployment of a portable, pencil-beam, pulsed, 3-cm Doppler radar. *J. Atmos. Oceanic Technol.,* **14,** 1502–1512, doi:10.1175/1520-0426(1997)014<1502:DADOAP>2.0.CO;2.

Yu, C.-K., and B. F. Smull, 2000: Airborne Doppler observations of a landfalling cold front upstream of steep coastal orography. *Mon. Wea. Rev.,* **128,** 1577–1603, doi:10.1175/1520-0493(2000)128<1577:ADOOAL>2.0.CO;2.